AN INVESTIGATION OF THE CONFINED VORTEX FLOW OF LIQUIDS

by

Essam Ahmed Farag

A THESIS
IN THE
FACULTY OF ENGINEERING

Presented in partial fulfilment of the requirements
for the
Degree of DOCTOR OF ENGINEERING
at
Sir George Williams University
Montreal, Canada

August 1971

To

My Parents

My Wife Hind

and

Dina and Ahmed

ABSTRACT

Theoretical and experimental investigations of the swirling flow of liquids within cylindrical chambers of high slenderness ratio were carried out. Two primary methods of inducing such flows were considered: (a) using tangential circumferential inlets, and (b) rotating the cylindrical chamber. Approximate analytical solutions of the boundary-layer thickness for each case were obtained by solving the boundary-layer momentum integral equations. The radial and tangential velocity distributions were expressed in power series, where the constants of the series were determined by the boundary conditions. The solutions were applied to predict the discharge coefficient at various coefficients of swirl.

Experimental investigations of the vortex flow were carried out to measure the actual discharge flow rate under different swirl conditions. A unique method was developed to measure the radial velocity profile of the liquid inside the chamber without affecting the actual flow pattern. For both flow cases, good agreement between theory and experimental results was obtained.

A detailed classification of vortex flow of liquids discharging into the atmosphere was carried out by the intro-

duction of the swirl coefficient $X = \Omega/a\sqrt{2gh}$. Four flow regimes covering the range from pure radial flow with zero swirl where $X = 0$, to strong swirl where $X \geqslant 1$, were defined. The approximate analytical solutions developed are applicable to both medium and high swirl conditions whereas the weak swirl flow was experimentally verified to resemble pure radial streaming flow.

ACKNOWLEDGEMENTS

The author wishes to express his gratitude to his advisor, Dr. C.K. Kwok, for his invaluable suggestions and encouragement during this investigation.

The author wishes to thank Dr. M.P. du Plessis for his helpful comments and encouragement and Mr. W.F. Hayes, Dr. Sui Lin and Mr. N. Suresh for their co-operation.

Special thanks are extended to Dr. M.N.S. Swamy and Dr. K. Foster for their valuable advice and suggestions during the preparation of this thesis.

Acknowledgement is also made to the staff of the Engineering Machine Shop for their construction of experimental apparatus.

Finally, the author is indebted to the National Research Council of Canada for financial support under Grant No. A7435.

TABLE OF CONTENTS

CHAPTER I

CHAPTER II

CHAPTER III

CHAPTER IV

CHAPTER V

CHAPTER VI

LIST OF FIGURES

FIGURE page

LIST OF PLATES

NOMENCLATURE

a	outlet radius
a	suffix relating to outlet radius
$A_{P.F.}$	area occupied by potential flow at outlet
b	air core radius
C_d	discharge coefficient
E	factor in assumed expression for u-velocity
g	gravity acceleration
h	half chamber height
H	supply pressure head
Q	volume flow rate
$Q_{B.L.}$	volume flow rate through boundary layer
$Q_{P.F.}$	volume flow rate through potential flow region
Q_K	volume flow rate of kerosene through outlet
r	radial distance from axis
R	vortex chamber radius
r, θ, y	cylindrical coordinates in boundary-layer analysis
u, v, w	radial, tangential and axial components of velocity in boundary layer
U, V, W	radial, tangential and axial components of velocity in potential flow outside boundary layer
X	swirl coefficient $= \Omega/(a\sqrt{2gH})$
z	kerosene depth inside vortex chamber
δ	boundary-layer thickness

δ_1	non-dimensional boundary-layer thickness
η	non-dimensional y-coordinate = y/δ
μ	dynamic viscosity
ν	kinematic viscosity = μ/ρ
ξ	non-dimensional radius = r/R
ρ	density
τ	shear stress on fluid
f,F,ϕ	functions
ω	angular velocity
Ω	circulation constant = Vr

CHAPTER I

INTRODUCTION

1.1 Statement of the Problem

Vortex flow phenomena occurring in nature, such as tornadoes and whirlpools, are unconfined and many studies, both theoretical and experimental, have been carried out on the subject (1-5). In the past 20 years, interest has been generated in the study of confined vortex flows. This is due to there being many useful applications of confined swirl flow phenomena. Recently, with the advent of fluid amplifier technology, a series of very interesting experimental discoveries has generated enthusiasm for further application of confined vortex motions. This investigation was stimulated by the utilization of vortex flow in the design of vortex rate sensors and amplifiers.

Vortex chambers, in general, have a cylindrical configuration with a central outlet and circumferential inlets. There are two methods of creating the swirl motion inside the vortex chamber: first, the swirl is introduced by supplying fluid to the interior of the chamber through tangential circumferential inlets as shown in Fig. 1-a. This technique is used in atomizers and cyclone separators as well as vortex valves. The alternate method of producing swirl flow is by rotating the chamber about its central axis as shown in Fig. 1-b. When the fluid enters the chamber through the radial guide vanes, it attains the same tangential velocity as that of the guide vanes. The vortex rate sensor utilizes the latter method in generating swirl motion. For convenience, the above techniques of creating swirl motion inside vortex chambers will be referred to as the stationary vortex chamber and the rotating vortex chamber, respectively.

In this thesis, a general analytical solution of the problem for both stationary and rotating vortex chambers is developed and the solution is verified with experimental results. The solution presented can be considered an explicit and applicable mathematical relationship between the various geometrical and physical parameters of confined vortex flow of liquids in cylindrical chambers.

Many swirling flow conditions have been investigated in detail and a vast amount of information on the subject has accumulated over past years (6-28). Numerous reviews on confined vortex phenomena (6-8) covering the various aspects of this problem are also available. It is therefore considered that another detailed review of this subject would be repetitious. Consequently, only a brief review of the methods and solutions most relevant to the present work will be given.

1.2 Scope of the Present Work

The results of this investigation are presented in the next four chapters.

Chapter II deals with the theoretical analysis of vortex flow in a stationary vortex chamber. Previous related work is cited first, following which the boundary-layer integral equations are employed to analyze the high as well as the medium swirls of liquids.

Chapter III provides the solution for rotating vortex chambers for which the procedure of Chapter II is applied but with the different boundary conditions prevailing due to rotation of the chamber.

In Chapter IV, early experimental results obtained for the swirling flow of liquids through stationary vortex chambers (9) are presented and are used to substantiate the theoretically predicted results described in Chapter II. In this experimental work, a unique technique using two immiscible liquids is applied to determine the core flow originating from the top boundary layer inside the vortex chamber, without disturbing the actual flow pattern.

In Chapter V, the apparatus and experimental techniques used for the investigation of swirling flow of liquids through rotating vortex chambers are presented. An experimental technique similar to that described in Chapter IV was used for measuring the radial velocity distribution inside the vortex chamber; the results are then used to verify the theory given in Chapter III.

The usefulness of the above-mentioned theoretical and experimental results will be critically assessed and conclusions drawn in Chapter VI. Appropriate work for further studies related to the subject will be outlined.

CHAPTER II

THEORETICAL MODEL OF THE SWIRLING FLOW OF LIQUIDS IN A STATIONARY VORTEX CHAMBER

2.1 Introduction

Early attempts to analyze vortex flow in a stationary chamber are based on inviscid flow theory. The inviscid theory of swirling flow of liquids exhausting into the atmosphere was first explained by Taylor (10). The numerical results of this inviscid theory are presented in Fig. 2 in the form of the two non-dimensional parameters, namely the discharge coefficient C_d and the swirl coefficient X. They are defined by

$$C_d = Q/(\pi a^2 \sqrt{2gH}) \qquad (2.1)$$

and

$$X = \Omega/(a\sqrt{2gH}) \qquad (2.2)$$

where Q is the actual discharge
Ω is the circulation
a is the outlet radius
H is the total pressure head.

The curve shows that at zero swirl (i.e. X = 0), the discharge coefficient C_d is equal to unity. This corresponds to pure streaming sink flow with maximum flow rate. On the other hand, when the coefficient of swirl reaches unity, the discharge coefficient tends to zero. Taylor commented that under such a condition, there is an air core occupying the whole outlet area, the discharge ceases to exist and the total pressure head is theoretically absorbed in imparting the tangential velocity. From the physical standpoint, the above explanation is difficult to comprehend because, at low swirls, the air core is not formed based on experimental observations, and the value of C_d in this range is very close to that at zero swirl. However, at high swirl, the discharge does not cease, which is in direct contradiction to Taylor's theory.

Taylor (11), in another attempt to analyze flow in atomizers, solved the laminar boundary-layer momentum integral equations using the Pholhausen method in predicting the radial and tangential velocity profiles. The final equations were solved numerically and the results are shown graphically in Fig. 3 for the dimensionless parameters δ_1 and ξ which are defined as $[\frac{\delta}{r_1} (\frac{\Omega}{\nu \sin \alpha})^{1/2}]$ and r_1/R_1, respectively. This solution considers high swirl cases where the discharge is fed by boundary-layer flow only.

Weber (12) obtained a solution for the turbulent boundary layer inside a conical surface due to swirl flow around the cone axis. In his analysis, the momentum integrals of the boundary layer were obtained by the use of the control volume concept. The velocity profiles inside the boundary layer were assumed to satisfy the one-seventh power law and the boundary conditions using the shear stress data obtained from the pipe flow experiments. Again, this solution has similar limitations to that of Taylor (2) regarding the degree of swirl.

Wormley (13) presented a momentum integral analysis for the swirling flow in a short vortex chamber. The analysis was developed with the aid of flow visualization photographs and considered the interaction which occurs between the potential flow and the turbulent boundary layers. The shear law adopted in his investigation was similar to that used by Prandtl in the study of turbulent flow over a flat plate.

Kwok (14) split the vortex into two parts. The first for the flow in the annular outer region where the axial velocity is zero, and the second in the inner part of the vortex where this component is significant. The two parts are matched at appropriate radius by assuming that the tangential velocity, the tangential shear stress and the static pressure are continuous.

In the analytical part of this work, the velocity profiles inside the boundary layer were expressed in power series where the coefficients were determined by the boundary conditions. This enables one to solve the laminar boundary-layer equations. Once the boundary-layer thickness is obtained, the area of potential flow at the outlet can be determined. Consequently, the discharge coefficient C_d can be estimated for different swirl flow conditions.

2.2 Boundary-Layer Theory for Swirling Liquids

When a non-swirling liquid approaches a central orifice in the bottom of a cylindrical chamber, it converges from all points upstream of this orifice. Due to no-slip conditions at the wall, the velocity decreases near the solid boundary. When the liquid is swirling, however, the fluid particles distant from the boundary move in the radial direction towards the outlet under the influence of the pressure gradient and the centrifugal force. Under medium and high swirl conditions, the centrifugal force field predominates. However, this centrifugal force field near the solid boundary is reduced because of the no-slip conditions at the wall, therefore most of the inward flow exists near the surface. Consequently, for high swirl, a condition can arise in which the whole of the outflow from the orifice is fed by the boundary-layer flow developed close to the top and bottom surfaces of the swirl chamber. The top boundary-layer flow is moved radially inward and then downward to the orifice through the core flow region, while the bottom boundary-layer current is moved radially inward and is discharged directly through the orifice around the core flow, as shown in Fig. 4.

Based on the above description, a theoretical solution for high swirls of liquids into the atmosphere is first presented. Once the solution is obtained, the boundary-layer thickness can be predicted and the solution further extended to cover swirl flows of different intensities.

2.3 Solution for the Laminar Boundary Layer Inside a Stationary Vortex Chamber at High Swirl

A solution for the growth of the laminar boundary layer of a viscous liquid at the top and bottom surfaces of a cylindrical vortex chamber is developed by use of the boundary-layer momentum integral equations. The liquid is considered to enter the chamber of radius R tangentially with angular velocity ω. In this solution for high swirl flow, all the inward flow is carried by the boundary layer, therefore the potential flow outside the boundary layer will have no radial component. Due to the law of conservation of angular momentum, the tangential velocity V in the potential flow region at any radius r is expressed as

$$V = \frac{\Omega}{r} \tag{2.3}$$

where Ω is the circulation constant.

The Navier-Stokes equations for steady motion of a viscous liquid in cylindrical coordinates are:

$$u\frac{\partial u}{\partial r} + \frac{v}{r}\frac{\partial u}{\partial \theta} - \frac{v^2}{r} + w\frac{\partial u}{\partial y} = -\frac{1}{\rho}\frac{\partial P}{\partial r} + \frac{1}{\rho}\frac{\partial \tau_r}{\partial y} \qquad (2.4)$$

$$u\frac{\partial v}{\partial r} + \frac{v}{r}\frac{\partial v}{\partial \theta} + \frac{uv}{r} + w\frac{\partial v}{\partial y} = -\frac{1}{\rho}\frac{\partial P}{\partial \theta} + \frac{1}{\rho}\frac{\partial \tau_\theta}{\partial y} \qquad (2.5)$$

$$u\frac{\partial w}{\partial r} + \frac{v}{r}\frac{\partial w}{\partial \theta} + w\frac{\partial w}{\partial y} = -\frac{1}{\rho}\frac{\partial P}{\partial y} + \frac{1}{\rho}\frac{\partial \tau_y}{\partial y} \qquad (2.6)$$

and the equation of continuity is

$$\frac{\partial u}{\partial r} + \frac{u}{r} + \frac{1}{r}\frac{\partial v}{\partial \theta} + \frac{\partial w}{\partial y} = 0 \qquad (2.7)$$

where r is the radius

u is the radial velocity component

v is the tangential velocity component

w is the axial velocity component

p is the static pressure

ρ is the density

For axially symmetric flow, all the derivatives with respect to θ will vanish. Following normal practice, the curvature normal to the plate of flow in the boundary-layer over a flat plate is assumed negligible so that $\partial P/\partial y = 0$; also, by estimate, terms of second order of magnitude are neglected. The foregoing equations can then be approximated as

$$u\frac{\partial u}{\partial r} + w\frac{\partial u}{\partial y} - \frac{v^2}{r} = -\frac{1}{\rho}\frac{\partial P}{\partial r} + \frac{1}{\rho}\frac{\partial \tau_r}{\partial y} \qquad (2.8a)$$

$$u\frac{\partial v}{\partial r} + w\frac{\partial v}{\partial y} + \frac{uv}{r} = \frac{1}{\rho}\frac{\partial \tau_\theta}{\partial y} \qquad (2.8b)$$

$$\frac{\partial u}{\partial r} + \frac{u}{r} + \frac{\partial w}{\partial y} = 0 \qquad (2.8c)$$

These expressions can be written in the integral form as:

$$\int_0^\delta \left(u\frac{\partial u}{\partial r} + w\frac{\partial u}{\partial y} - \frac{v^2}{r}\right)dy = \frac{1}{\rho}\int_0^\delta \left(-\frac{\partial P}{\partial r} + \frac{\partial \tau_r}{\partial y}\right)dy \qquad (2.9)$$

$$\int_0^\delta \left(u\frac{\partial v}{\partial r} + w\frac{\partial v}{\partial y} + \frac{uv}{r}\right)dy = \frac{1}{\rho}\int_0^\delta \left(\frac{\partial \tau_\theta}{\partial y}\right)dy \qquad (2.10)$$

where δ is the boundary-layer thickness.

Integrating eqn. 2.8c

$$w = -\int_0^y \left(\frac{\partial u}{\partial r} + \frac{u}{r}\right) dy \qquad (2.11)$$

The momentum equation for the potential flow outside the boundary layer with zero radial velocity may be expressed as

$$\frac{1}{\rho}\frac{\partial P}{\partial r} = \frac{\Omega^2}{r^3} = \frac{(\varpi R^2)^2}{r^3} \qquad (2.12)$$

Substituting for w and $\partial P/\partial r$ in eqns. 2.9 and 2.10, and using the condition of zero shear stress at $\eta = 1$, the momentum integral equations across the boundary layer become:

$$\delta\int_0^1 \frac{\partial u^2}{\partial r}d\eta - \frac{\delta}{r}\int_0^1 (v^2 - u^2)\,d\eta - U\delta\int_0^1 \left(\frac{\partial u}{\partial r} + \frac{u}{r}\right)d\eta$$
$$= -\delta\frac{(\varpi R^2)^2}{r^3} + \frac{1}{\rho}\left|\tau_r\right|_{\eta=0} \qquad (2.13)$$

and

$$\delta\int_0^1 \frac{\partial uv}{\partial r}d\eta + 2\delta\int_0^1 \frac{uv}{r}d\eta - V\delta\int_0^1 \left(\frac{\partial u}{\partial r} + \frac{u}{r}\right)d\eta$$
$$= \frac{1}{\rho}\left|\tau_\theta\right|_{\eta=0} \qquad (2.14)$$

where $U = 0$ is the radial velocity outside the boundary layer

$V = \varpi R^2/r$ is the tangential velocity outside the boundary layer

$\eta = y/\delta$

In order to obtain a solution to eqns. 2.13 and 2.14, the radial and tangential velocity profiles must be specified. In this investigation, the radial and tangential velocity profiles are assumed to have the form

$$u/V = f(\eta) \qquad \text{and} \qquad v/V = \phi(\eta) \tag{2.15}$$

where $f(\eta)$ and $\phi(\eta)$ are assumed to be functions only of $\eta = y/\delta$ and must satisfy the boundary conditions.

Expanding $f(\eta)$ and $\phi(\eta)$ in two power series, which converge for $0 < \eta < 1$, the total number of terms considered in each series being dependent on the total available boundary conditions, we obtain two polynomial approximations as follows:

$$\frac{u}{V} = f(\eta) = (a_0 + a_1\eta + a_2\eta^2 + a_3\eta^3) \tag{2.16}$$

and

$$\frac{v}{V} = \phi(\eta) = (b_0 + b_1\eta + b_2\eta^2) \tag{2.17}$$

where the truncation errors are $\eta^4/4!u^{(4)}(\xi)$ and $\eta^3/3!v^{(3)}(\xi)$, $0 < \xi < \eta$. In order to evaluate the constants of the polynomial for the radial velocity distribution given by eq. 2.16, the following boundary conditions are used:

$$\text{at } \eta = 0 \;,\; u = 0 \text{ and } \nu\frac{\partial^2 u}{\partial y^2} = -\frac{(\omega R^2)^2}{r^3}$$

and (2.18)

$$\text{at } \eta = 1 \;,\; u = 0 \text{ and } \frac{\partial u}{\partial y} = 0$$

The constants of the polynomial for the tangential velocity distributions can be found by using the following boundary conditions:

$$\text{at } \eta = 0 \;,\; v = 0$$

and (2.19)

$$\text{at } \eta = 1 \;,\; \frac{\partial v}{\partial y} = 0 \text{ and } v = V = \frac{\omega R^2}{r}$$

Hence, the radial and tangential velocity distributions in the boundary layer will be respectively:

$$u = \frac{\Omega}{r} E(\xi)(\eta - 2\eta^2 + \eta^3) \tag{2.20}$$

and

$$v = \frac{\Omega}{r}(2\eta - \eta^2) \tag{2.21}$$

where $E(\xi) = \dfrac{\omega \delta^2}{4 \nu \xi^2}$ and $\xi = r/R$

With the assumed velocity profiles for u and v the wall shear stresses may be simplified and expressed in terms of δ by evaluating the gradients of u and v in the y-direction at the chamber wall as shown in reference (12) for the laminar case. Hence, the wall shear stress in the radial direction is given by:

$$\begin{aligned} \tau_r \Big|_{y=0} = \mu \left(\frac{\partial u}{\partial y}\right)_{y=0} &= \frac{\mu}{\delta}\left(\frac{\partial u}{\partial \eta}\right)_{\eta=0} \\ &= -\frac{\mu \Omega E}{\delta r} \end{aligned} \tag{2.22}$$

and the wall shear stress in the tangential direction is given by:

$$\begin{aligned} \tau_\theta \Big|_{y=0} = \mu \left(\frac{\partial v}{\partial y}\right)_{y=0} &= \frac{\mu}{\delta}\left(\frac{\partial v}{\partial \eta}\right)_{\eta=0} \\ &= -\frac{2\mu \Omega}{\delta r} \end{aligned} \tag{2.23}$$

The velocity profiles described by eqns. 2.20 and 2.21 are approximate and restrictive because of the choice of the particular polynomials. If the profiles were accurate, substituting them in eqns. 2.13 and 2.14 would yield exactly the same boundary-layer thicknesses. Therefore a check on accuracy will be to substitute the approximate profiles into these equations and to compare the results with respect to the boundary-layer thickness.

Substituting the velocity profiles given by eqns. 2.20 and 2.21 into eqn. 2.13, one obtains:

$$\frac{d\delta^2}{d\xi} = -406\left(\frac{\nu}{\omega}\right)^2 \frac{\xi^3}{\delta^2} + \frac{5}{2}\,\frac{\delta^2}{\xi}$$

Rearranging the above differential equation, putting $\delta^4 = K$

$$\frac{1}{2}\,\frac{dK}{d\xi} - \frac{5}{2}\,K\left(\frac{1}{\xi}\right) = -406\left(\frac{\nu}{\omega}\right)^2 \xi^3$$

hence, multiplying both sides by $1/\xi^5$, one obtains:

$$\frac{d}{d\xi}\left(\frac{K}{\xi^5}\right) = -812\left(\frac{\nu}{\omega}\right)^2 \frac{1}{\xi^2} \qquad (2.24)$$

The last differential equation is solved mathematically in a closed form using the boundary condition at $\xi = 1$, $K = 0$. The expression for δ obtained from eq. 2.24 is given by

$$\delta = \xi\left(\frac{812\,\nu^2}{\omega^2}\right)^{1/4}(1-\xi)^{1/4} \qquad (2.25)$$

Similarly, substituting the velocity profiles given by eqns. 2.20 and 2.21 into eqn. 2.14, one obtains:

$$\frac{d\delta^2}{d\xi} = -240\left(\frac{\nu}{\omega}\right)^2 \frac{\xi^3}{\delta^2} + 2\,\frac{\delta^2}{\xi}$$

Rearranging the above differential equation, putting $\delta^4 = K$

$$\frac{1}{2}\,\frac{dK}{d\xi} - 2K\left(\frac{1}{\xi}\right) = -240\left(\frac{\nu}{\omega}\right)^2 \xi^3$$

hence multiplying both sides by $1/\xi^4$, one obtains

$$\frac{d}{d\xi}\left(\frac{K}{\xi^4}\right) = -480\left(\frac{\nu}{\omega}\right)^2 \frac{1}{\xi} \qquad 2.26$$

The last differential equation is solved mathematically in a closed form using the boundary condition at $\xi = 1$, $K = 0$. The expression for δ obtained from eqn. 2.26 is given by:

$$\delta = \xi \left(\frac{480\,\nu^2}{\omega^2}\right)^{1/4} \left(-\ln\xi\right)^{1/4} \qquad (2.27)$$

The results of eqns. 2.25 and 2.27 are presented graphically in Fig. 5 for the two dimensionless quantities $\delta/\sqrt{\nu/\omega}$ and ξ. It is seen that the boundary-layer thickness starts from zero at the periphery of the chamber and increases rapidly in the direction of flow. The boundary-layer thickness given by eqn. 2.25 reaches it maximum at $\xi = 0.80$, while the boundary-layer thickness given by eqn. 2.27 reaches its maximum at $\xi = 0.78$. At $\xi = 0$, which corresponds to the centre of the vortex chamber, the results indicate that the boundary-layer thickness is zero. Physically, this is precisely what should have happened. The boundary layer at the leading edge or periphery of the vortex chamber should be zero and should increase gradually in the direction of flow. Once the maximum boundary layer is reached, δ starts to decrease. This may be explained by the fact that when the fluid is moving towards the central exhaust, a more favourable pressure gradient develops due to the rapid increase in magnitude of both the tangential and radial velocity components. This is analogous to the case of accelerated fluid flow in a convergent channel*.

It may be observed from Fig. 5 that the two curves for δ do not overlap each other which should have been the case if the velocity profiles had been obtained by solving eqns. 2.8a,

---

*Boundary-Layer Theory by H. Schlichting, 6th ed., McGraw-Hill, 1968, p. 152.

2.8b and 2.8c simultaneously. However, the discrepancy between the two curves for δ is not great even though the profiles for u and v are approximate. In fact, the maximum deviation between the two curves is 12% near the periphery. Hence, from an engineering design point of view, either of the two curves for δ and hence either of the expressions in eqns. 2.25 and 2.27 can be used. To justify this statement, these curves are compared, in Fig. 5, with that of Taylor (11), where the half cone angle α is assumed to be 90°. It may be observed from Fig. 5 that the three profiles have the same trend of variation, except that eqns. 2.25 and 2.27 predict higher values of δ than those of Taylor, with a maximum percentage difference of 65% of Taylor's profile at $\xi = 0.6$. To further justify the theoretical results obtained for δ in this thesis, the coefficient of discharge calculated using δ as given by eqn. 2.25 is compared in Chapter IV with experimental observations.

2.4 Application of the Laminary Boundary-Layer Solution to Predict Discharge Coefficient at High Swirl

Once the expression δ is found, the boundary-layer flow ($Q_{B.L.}$) on the bottom plate of a cylindrical vortex chamber can be calculated at the outlet radius a. This boundary-layer flow is given by:

$$
\begin{aligned}
Q_{B.L.} &= \int_0^\delta 2 \pi a\, u\, dy \\
&= 2 \pi a\, \delta_a \int_0^1 u\, d\eta \qquad (2.28)
\end{aligned}
$$

Substituting the radial velocity distributions given by eqn. 2.22 at the outlet radius, one obtains:

$$Q_{B.L.} = \frac{\pi}{24\nu} \delta_a^3 \left(\frac{\omega R}{\xi_a}\right)^2 \tag{2.29}$$

where $\xi_a = a/R$ and δ_a is the boundary-layer thickness at the outlet radius a.

Since the vortex chambers considered are relatively short (i.e. h is small), the pressure on the top and bottom boundaries may be considered the same. Hence, the total outflow from the outlet will be:

$$Q = \frac{\pi}{12\nu} \delta_a^3 \left(\frac{\omega R}{\xi_a}\right)^2 \tag{2.30}$$

Dividing each side of eqn. 2.28 by $(\pi a^2 \sqrt{2gH})$, it can be written in a dimensionless form as:

$$C_d = \omega^2 \delta_a^3 / (12 \nu \xi_a^4 \sqrt{2gH}) \tag{2.31}$$

2.5 Solution for Swirling Flows Through Stationary Vortex Chambers at Medium Swirl

Medium swirls can be defined as those in which the whole outflow from a vortex chamber is fed by the boundary-layer currents and the potential flow provided that an air core exists, at least at the outlet, as illustrated in Fig. 6. For a large slenderness ratio with small vortex chamber height, as soon as the top and bottom boundary-layer flows reach the outlet radius, they separate from the boundary to fall freely into the atmosphere. Consequently, the mean axial velocity in the boundary layer at the outlet may be considered equal to the mean radial component of velocity across the boundary layer at the outlet radius; hence, the area of potential flow at the outlet will be:

$$A_{P.F.} = \pi (a^2 - 4 a \delta_a - b^2) \tag{2.32}$$

where $A_{P.F.}$ is the area occupied by the potential flow at the outlet

δ_a is the boundary-layer thickness at the outlet radius

b is the aire-core radius at the outlet.

The radial component of velocity, U, is very small compared with the other two components. Hence, for the potential flow region, the inviscid momentum equation at the outlet is given by:

$$H = \frac{W^2 + V^2}{2g} \tag{2.33}$$

wherw H is the total pressure head at the outlet level

W is the axial velocity of the potential flow through the outlet

and V is the tangential velocity of the potential flow at r = b + s as shown in the figure.

Hence, from the law of conservation of angular momentum, one obtains:

$$V^2 = \left(\frac{\omega R^2}{b + \delta} \right)^2 = \frac{\omega^2 R^4}{b^2 + 2 a \delta_a} \tag{2.34}$$

Combining eqns. 2.32, 2.33 and 2.34, the expression for the potential flow rate through the outlet may be expressed as follows:

$$Q_{P.F.} = \pi\left(a^2 - 4a\delta_a - b^2\right)\left(2gH - \frac{\omega^2 R^4}{b^2 + 2a\delta_a}\right)^{1/2} \qquad (2.35)$$

The condition for $Q_{P.F.}$, at a certain angular velocity, to have maximum value is $d/db(Q_{P.F.}) = 0$. This gives

$$b^6 + \left(2a\delta_a - \frac{\omega^2 R^4}{4gH}\right)b^4 + \frac{\omega^2 R^4}{4gH}\left(6a\delta_a - a^2\right)b^2 - \frac{\omega^2 R^4}{4gH}\left(2a\delta_a\right)\left(a^2 - 4a\delta_a\right) = 0 \qquad (2.36)$$

which is a cubic equation in b^2. Generally, the solution of eqn. 2.36 has one real root and two imaginary roots for b^2. In applying this equation for calculating the air core radius, only positive real roots have to be considered.

Hence, the total volume flow rate through an outlet of a stationary vortex chamber can be found to be the sum of the flow due to boundary-layer and potential flow regions. Therefore, by combining eqns. 2.30 and 2.35, one obtains:

$$Q = \frac{\pi}{12\nu}\left(\frac{\omega R}{\xi_a}\right)^2 \delta_a^3 - \pi\left(a^2 - 4a\delta_a - b^2\right)\left(2gH - \frac{\omega^2 R^4}{b^2 + 2a\delta_a}\right)^{1/2} \qquad (2.37)$$

Dividing eqn. 2.37 by $\pi a^2 (2gH)^{1/2}$, the general expression for the coefficient of discharge, C_d, at medium and high swirls is given by:

$$C_d = \frac{\frac{\delta_a^3}{12\nu}\left(\frac{\omega R}{\xi_a}\right)^2 + \left(a^2 - 4a\delta_a - b^2\right)\left(2gH - \frac{\omega^2 R^4}{b^2 + 2a\delta_a}\right)^{1/2}}{a^2 (2gH)^{1/2}} \qquad (2.38)$$

A careful examination of the potential flow term in the foregoing equation shows that this term vanishes at $X = 1.0$. This indicates that there is no potential flow through the outlet at $X \geq 1.0$, and the whole outflow is fed by the boundary layers. Hence, $X = 1.0$ can be considered as the start of high swirl.

CHAPTER III

THEORETICAL MODEL OF THE VORTEX FLOW OF LIQUIDS IN A ROTATING VORTEX CHAMBER

3.1 Introduction

Theoretical analysis carried out for stationary vortex chambers cannot be applied to rotating vortex chambers because of the different boundary conditions resulting from rotation of the top and bottom boundaries of the chamber.

Relatively little previous theoretical work has been carried out for rotating vortex chambers. Sarpkaya (24) assumed very low swirl conditions, treating flow inside the vortex chamber in the same way as an unaccelerated fluid flow on a flat plate at zero incidence which eventually led to the solution of pure radial flow. The solution showed that the leading edge of the boundary at the periphery of the chamber is effectively a ring of singularity with maximum boundary-layer thickness at the inner face of the coupling. Physically, it is quite difficult to envisage the existence of such a boundary-layer configuration. Later, the same author (25) improved the analysis and presented the development of the boundary layer starting from zero at the periphery. The solution applies only to pure radial flow and is limited to the application of very weak swirl flow conditions.

Neradka (26) obtained another solution for the laminar boundary layer, using Mangler's transformation* for axially symmetrical boundary layers. The solution neglected completely the tangential velocity component.

In the present solution for vortex flow inside a rotating chamber, a procedure similar to that of Chapter II is carried out by considering both the tangential and radial velocities. Power series expansion for the radial and tangential velocity profiles inside the boundary layer is developed using the available boundary conditions.

3.2 Solution for the Laminar Boundary Layer Inside a Rotating Vortex Chamber at High Swirl

For vortex flow generated by the rotation of the chamber, the boundary condition is different from that of the stationary case. Due to the no-slip condition, the fluid at the boundary must move at the same velocity as that of the chamber boundaries which rotate with constant angular velocity ω around the axis of the chamber.

The velocity distributions in the boundary layer are assumed to have the same general form as given by eqns. 2.16 and 2.17 for the radial and tangential components of velocity, respectively.

A new set of boundary conditions is used to evaluate

---

*Boundary-Layer Theory by H. Schlichting, 6th ed., McGraw-Hill 1968, p. 235.

the constants of the polynomials assumed. For the radial velocity distribution, the following boundary conditions are used:

$$\text{at} \quad \eta = 0 \,, \quad u = 0 \quad \text{and} \quad \frac{\partial^2 u}{\partial y^2} = -\frac{\omega^2}{\nu r^3}(R^4 + r^4)$$

and (3.1)

$$\text{at} \quad \eta = 1 \,, \quad u = 0 \quad \text{and} \quad \frac{\partial u}{\partial y} = 0$$

For the tangential velocity distribution, the following boundary conditions are used:

$$\text{at} \quad \eta = 0 \,, \quad v = \omega r$$

and (3.2)

$$\text{at} \quad \eta = 1 \,, \quad \frac{\partial v}{\partial y} = 0 \quad \text{and} \quad v = V = \frac{\omega R^2}{r}$$

Hence, the radial and tangential velocity distributions in the boundary layer are, respectively,

$$u = \frac{\Omega}{r} E(\xi)(\eta - 2\eta^2 + \eta^3) \qquad (3.3$$

where $E = \dfrac{\omega \delta^2}{4 \nu \xi^2} \quad (\xi^4 + 1)$

and $$v = \frac{\Omega}{r}\left[\xi^2 - 2(\xi^2 - 1)\eta + (\xi^2 - 1)\eta^2\right] \qquad (3.4)$$

Substituting the velocity profiles given by eqns. 3.3 and 3.4 into eqn. 2.13, one obtains:

$$\frac{dE^2}{d\xi} = -\frac{49}{\xi} + \frac{E^2}{\xi} - \frac{105(1 + \xi^4)}{4\xi} + 7\xi(3\xi^2 + 4)$$

Rearranging the above differential equation,

$$\frac{dE^2}{d\xi} - \frac{E^2}{\xi} = -\left(\frac{301}{4}\right)\frac{1}{\xi} + 28\xi - \frac{21}{4}\xi^3$$

hence multiplying both sides by $1/\xi$, one obtains:

$$\frac{d}{d\xi}\left(\frac{E^2}{\xi}\right) = -\left(\frac{301}{4}\right)\frac{1}{\xi^2} + 28 - \frac{21}{4}\xi^2 \qquad (3.5)$$

The above differential equation is solved mathematically in a closed form using the boundary condition at $\xi = 1$, $E = 0$, and the equation for the boundary-layer thickness is given by:

$$\delta = 2\xi \left(\frac{\nu}{\omega}\right)^{1/2} \left[\frac{\frac{301}{4} + 28\,\xi^2 - \frac{7}{4}\xi^4 - \frac{203}{2}\xi}{(1+\xi^4)^2} \right]^{1/4} \qquad (3.6)$$

The solution for is presented graphically in Fig. 7 for the two dimensionless quantities $\delta/\sqrt{\nu/\omega}$ and ξ. This shows that the boundary layer starts with zero thickness at the periphery and increases in the direction of flow, reaching its maximum value at $\xi = 0.69$. It then decreases again and approaches zero thickness at the axis of the chamber. These trends to the development of the boundary layer can again be interpreted from a physical standpoint.

3.3 Application of the Laminary Boundary-Layer Solution to Predict the Discharge Coefficient at High Swirl

By integrating the radial velocity distribution across the boundary-layer thickness at the outlet radius, the volume flow rate can be expressed as:

$$Q_{B.L.} = \frac{\pi}{24\nu} \left(\frac{\omega R}{\xi_a}\right)^2 (1 + \xi_a^4)\, \delta_a^3 \qquad (3.7)$$

Since the vortex chamber height (2h) is small in comparison to the radius, it is possible to consider that the pressure distributions at the top and bottom boundaries are the same. Hence, the total outflow from the outlet becomes:

$$Q = \frac{\pi}{12\nu}\left(\frac{\omega R}{\xi_a}\right)^2 (1 + \xi_a^4)\,\xi_a^3 \qquad (3.8)$$

Dividing the foregoing equation by $\pi a^2(2gH)^{1/2}$, the expression for the coefficient of discharge becomes:

$$C_d = \omega^2 \xi_a^3 (1 + \xi_a^4) \big/ (12\,\nu\,\xi_a^4 \sqrt{2gH}) \qquad (3.9)$$

3.4 Solution for Swirling Flows Through Rotating Vortex Chambers at Medium Swirl

The assumptions and solution for the potential flow given in Section 2.5 can be applied. Combining the general eqn. 2.35 for the flow rate in the potential flow region and the boundary-layer flow rate defined by eqn. 3.8, the expression for the total outflow can be written as:

$$Q = \frac{\pi}{12\nu}\left(\frac{\omega R}{\xi_a}\right)^2 (1 + \xi_a^4)\,\xi_a^3 + \pi(a^2 - 4a\xi_a - b^2)\left(2gH - \frac{\omega^2 R^4}{b^2 + 2a\xi_a}\right)^{1/2} \qquad (3.10)$$

Dividing eqn. 3.10 by $\pi a^2(2gH)^{1/2}$, the following expression for the coefficient of discharge is obtained

$$C_d = \frac{\frac{\xi_a^3}{12\nu}\left(\frac{\omega R}{\xi_a}\right)^2 (1 + \xi_a^4) + (a^2 - 4a\xi_a - b^2)\left(2gH - \frac{\omega R^4}{b^2 + 2a\xi_a}\right)^{1/2}}{a^2 (2gH)^{1/2}} \qquad (3.11)$$

It was found that the potential flow term in the foregoing equation vanishes at X = 1.0, indicating the upper limit of medium swirl and the start of high swirl.

CHAPTER IV

EXPERIMENTAL INVESTIGATION OF THE SWIRLING FLOW OF LIQUIDS THROUGH STATIONARY VORTEX CHAMBERS

4.1 Introduction

To supplement the analytical work presented in Chapter II for the stationary vortex chamber, the experimental results of the author (9) are briefly reviewed in this chapter. The results are used to substantiate the analytical solution given by eqn. 2.38.

The author (9) studied the factors that might affect the swirling flow of liquids from a stationary vortex chamber through a central outlet located at the bottom of the chamber. The factors examined are those which govern the geometry of the swirl chamber, namely:

i - The radius ratio, (R/a), which is the ratio of the vortex chamber radius to the outlet radius.

ii - The slenderness ratio, (R/h), which is the ratio between the diameter and the height of the vortex chamber.

The flow pattern inside the vortex chamber has been examined and a further study of the different shapes of the issuing jet was carried out. The percentage of core flow originating from the top boundary layer in the total outflow was determined by a unique technique using two immiscible liquids.

4.2 Experimental Model

A plexiglass cylinder, 10 inches long, 4 inches internal diameter and with a wall 0.25 inch thick, was supported vertically on a ball-bearing inside an open tank as shown in Fig. 8. The cylindrical tank was of glass. In the revolving cylinder, 720 holes of 0.25 inch diameter were drilled in 20 staggered rows 0.4 inch apart. The cylinder was rotated by a belt driven by a 1/2 horsepower electric D.C. motor through a reduction gear. Water was admitted between the rotating cylinder and the glass tank and was controlled by a regulating valve. Between the valve and the apparatus there was a small tank with a weir which maintained a steady level in the glass tank. The outlets could be installed at a central opening in the bottom of the chamber.

In order to simulate a closed vortex chamber, a smooth circular brass disc, 3.86 inches diameter and 0.15 inch thick, was concentrically placed inside the perforated cylinder. The design allowed easy adjustment of the level of the brass plate. To examine the flow pattern inside the cylinder, a solution of permanganate in water was injected into the interior of the swirl chamber at the top, bottom and side of the chamber as shown.

4.3 Experimental Procedure

The experimental procedure consisted of adjusting the water level inside the glass tank and altering the speed of rotation of the perforated cylinder in steps. At each step, the rate of discharge and the speed of rotation were recorded. The revolutions were timed with a stop-watch and the water, after passing through the outlet, was measured by volume for a known time. The tangential velocity of the swirl imposed on the water on admission to the interior of the cylinder was equal to that of the inner surface of the chamber.

The procedure was used in testing three outlet orifices of 0.189, 0.321 and 0.489 inch diameter at three vortex chamber heights, 7.0, 4.2 and 2.2 inches. The results were presented graphically in the form of the two non-dimensional parameters, namely, the discharge coefficient, C_d, and the swirl coefficient, X, defined by eqns. 2.1 and 2.2 respectively. The range of experiments covered the values of X from zero to 1.6, while the water temperature was varied between 65° and 70°F.

4.4 General Description of the Swirling Flow of Liquids

The experimental results indicate that swirling flows with non-merging boundary layers inside the vortex chamber may be classified in the following four well-defined phases of flow:

i - Weak Swirl: at which there is no air core and the tangential velocity at the outlet is very small compared with the axial component of velocity. The value of C_d during this phase varies according to the shape and diameter of the outlet following the known trend given in texts for low values of Reynolds number at zero swirl*

ii - <u>Critical Swirl</u>: at which the tangential velocity at the outlet of the chamber reaches a critical value such that the available supply pressure head is equal to that of the velocity. During this short flow phase, the vertex of the air core inside the emergent jet tries to force its way up into the outlet. This phase of swirling flow is quite unsteady.

iii - <u>Medium Swirl</u>: which is bounded by the point at which the air core establishes itself at the outlet and the point at which the swirl coefficient is equal to unity (i.e. $X = 1$). During this flow phase, the coefficient of discharge is decreased substantially and the air core may be developed inside the chamber depending on the size of the outlet.

iv - <u>High Swirl</u>: during which the potential flow inside the chamber ceases to feed the outlet and the whole outflow is fed by the boundary layers. This phase starts when the swirl coefficient is equal to unity as indicated by the theoretical solution given by eqns. 2.37 and 3.10.

---

*Fluid Mechanics, Victor L. Streeter, McGraw-Hill, 4th ed., p. 420.

This is a first attempt to classify the different flow regimes encountered in the swirling flow of liquids into the atmosphere. Once these phases are defined, the different flow configurations can be treated in a rigorous manner.

4.5 Effect of Radius Ratio

The three outlet orifices mentioned in Section 4.3 were tested. The smooth brass top plate is set at a height of 7.0 inches above the bottom of the chamber maintaining a constant slenderness ratio of 0.59. The water level inside the glass tank is adjusted to maintain a constant pressure head, H, of 8.0 inches of water above the outlet. The procedure described in Section 4.3 is then followed by gradually increasing the swirl.

The results are presented in Fig. 9 for the three radius ratios 20.0, 12.5 and 8.3. The figure shows the same trend of variation of C_d with X described in Section 4.4, i.e., the value of C_d remains nearly constant until an air core is formed, and then decreases with increase of X. At medium and high swirls, there is a tendency toward higher discharge coefficients for smaller outlet diameter, as indicated. This corresponds to the prediction of the solution given by eqn. 2.38.

The discontinuity observed at X = 0.68 on the curve for the 12.5 radius ratio is found to occur at the point where the air core becomes fully developed. This discontinuity does not appear in Fig. 10 where the test is carried out in the reverse direction beginning with the maximum value of X, with the air core fully developed, and then decreasing the swirl in steps. On investigation, it is observed that when the air core is formed at the outlet, its top is nearly spherical in shape, as shown in Fig. 11-a. This air core configuration is believed to obstruct the flow more than does the air core when it is fully developed, as shown in Fig. 11-b. The discontinuity is not observed for the case where the radius ratio is equal to 20.0 because the air core was never fully developed. For the case where the radius ratio is equal to 8.3, the range for the development of the air core right up to its fully developed configuration is so short that the exact transition point cannot be detected experimentally.

4.6 Effect of Slenderness Ratio

The three outlets were tested at the three slenderness ratios 0.59, 0.95 and 1.81. Sample results are presented in Fig. 12 for the radius ratio 8.3. These results show that at medium swirls, lower values of the discharge coefficient are obtained as the slenderness ratio is increased. This decrease in the discharge coefficient at medium swirls is due to the reduction of the area of potential flow inside the chamber. This reduction in area at any radius inside the chamber does not affect the outflow at high swirls because the potential flow ceases to feed the outlet and the outlet is only fed by the boundary layer.

4.7 Flow Pattern

Examination of the flow pattern inside the vortex chamber at various conditions during experimentation shows that, at the early stages of medium swirls, the top boundary-layer flow moves radially inwards and then downwards to the central outlet through the core flow region, while the bottom boundary-layer flow moves radially inwards and discharges directly through the outlet, as shown diagramatically in Fig. 13-a. As the swirl is increased, the boundary-layer flow increases to a limit beyond which the outlet cannot drain all the boundary-layer flow. This throttling effect creates a back-pressure which causes the boundary layer to separate. The separation of the bottom boundary layer occurs first in the form of a reversed upward flow in a thin zone around the core flow region, as shown in Fig. 13-b. As a consequence of the pressure build-up around the exit region, the separation of the top boundary layer occurs eventually resulting in the complex flow phenomena shown in Fig. 13-c.

4.8 Determination of the Core Flow

In order to measure directly the percentage of the core flow originating in the top boundary layer to the total flow through the outlet, another liquid, immiscible in and lighter than water, is simultaneously supplied to the apparatus. Commercial kerosene was chosen because most of its properties are closer to those of water than any other available oil. The kerosene supplied to the apparatus with water floats on the water and the top plate is immersed in it. Using a constant depth of kerosene of the order of 2 inches, which is greater than the maximum boundary-layer thickness predicted by Taylor (11), all the kerosene draining through the outlet will be coming from the top boundary layer. Therefore, in order to measure this core flow, a sample of the outflow is collected in a given interval, the percentage of core flow to total outflow being equal to the percentage of kerosene in the sample collected.

Sample results are presented in Fig. 14 in which the total discharge is plotted against the swirl coefficient; the amount of kerosene is then subtracted from the total discharge. The core flow as a percentage of the total flow is shown in Fig. 15 indicating that the percentage of kerosene in the total outflow is zero at zero swirl, increasing as swirl increases until it reaches a constant value of 60% at X = 0.9. Theoretically, this percentage should be 50% for a homogeneous liquid at high slenderness ratio. The 10% increase in kerosene flow can be attributed to the difference between the viscosity of water and kerosene. In addition, the small slenderness ratio (R/h = 0.59) causes a slightly different pressure distribution between the top and bottom surfaces of the experimental chamber. Nevertheless, the results provide an excellent qualitative insight into the complex flow phenomena without disturbing the flow.

4.9 Comparison Between Theory and Experimental Results

Applying eqn. 2.38 for the coefficient of discharge through stationary vortex chambers to the vortex chamber described in Section 4.2, the parameters substituted are:

$\nu = 10.9 \times 10^{-6}$ ft^2/sec
H = 0.667 ft of water
a = 0.2445 inch
R = 2.0 inch
$\zeta_a = 0.2445$
g = 32.2 ft^2/sec

and the coefficient of discharge is then calculated for different values of ω. The results are presented in Fig. 16 together with the experimental results for the two non-dimensional quantities C_d and X. The theory shows that at medium swirls, the discharge coefficient decreased as the swirl increased until X = 1, at which the potential flow ceases to feed the outlet. The differences between the theory and experimentally measured data are expected to be further reduced for tests carried out using large slenderness ratios, since the theory assumes equal pressure distribution on the top and bottom plates.

At high swirls, starting from X = 1.0, the discharge coefficient increases slowly as the swirl increases due to the growth of the boundary-layer flow which feeds the outlet. In fact, this slow increase predicted by the theory at high swirls would not actually occur because the effect of flow velocities on the variation of air core diameter is not considered in the theory at high swirls. It is expected that when X is increased, the reduction of static pressure near the core region will cause a further increase in the air core diameter. This creates a throttling effect on the flow and results in a further reduction of flow rate. However, this effect is quite small, as can be seen from the actual experimental data.

In order to verify the theoretically predicted boundary-layer profile, experimental readings for the total outflow rate at high swirls are used to calculate at different radii using eqn. 2.30. A sample of these data calculated from experimentally measured values is shown in Fig. 17, in which two values are used covering the case for the 0.321 and 0.489 inch diameter outlet orifices at X = 1.0. The results show excellent agreement except at the points near the periphery. From the theoretical standpoint, the boundary-layer thickness δ must equal zero at the periphery, and this is actually one of the boundary conditions used in the analysis. However, in the high swirl analysis it is also assumed that all the flow must be carried out by the boundary layer. It is obvious that somewhere within the chamber, very near the periphery, the fluid is directed towards the boundary layers. However, this particular region is not of great interest in the present study.

CHAPTER V

EXPERIMENTAL INVESTIGATION OF THE SWIRLING FLOW OF LIQUIDS THROUGH ROTATING VORTEX CHAMBERS

5.1 Introduction

In order to verify the proposed mathematical solution presented in Chapter III for the rotating vortex chamber, the following experimental work was carried out. In the experimental investigation, the following factors were examined:

i - the radius ratio, R/a

ii - the slenderness ratio, R/h

iii - the supply pressure head.

Any fluid flow, in particular swirling flow, is very sensitive to disturbance. The effect is further magnified because of the physical limitations of the experimental chamber. In general, a probe introduced into the flow region will drastically affect the flow pattern. The strong intensity of the swirl will render the measuring problem more acute. The techniques of using pitot tubes or hot wires were not considered because of the anticipated disturbance caused by the physical size of the measuring probe. The technique of the two immiscible liquids described in Section 4.8 for measuring the core flow was applied to measure the radial velocity distribution inside the vortex chamber. In addition, flow visualization techniques using colour injection into the chamber were carried out.

5.2 Experimental Model

A vortex chamber consisting of two aluminum circular plates 7.5 inches in diameter with 30 plexiglass radial vanes is supported vertically on a thrust bearing inside a cylindrical plexiglass tank as shown in Fig. 18. Each vane is 0.75 inch wide, 8.50 inches high and 0.187 inch thick. A smooth aluminum disc, 5.95 inches in diameter and 0.25 inch thick, which forms the top plate of the vortex chamber, is concentrically placed inside the chamber with a half-inch diameter stainless steel rod fixed vertically to its centre. This rod is used to locate the exact position of the plate. The vortex chamber is belt-driven using a one horsepower electric D.C. motor coupled to a reduction gear box. Water is admitted into the annular region between the rotating vortex chamber and the plexiglass tank. The flow rate is controlled by means of a needle valve. Two rounded outlets of 0.25 and 0.5 inch diameter were made. The central opening in the bottom of the chamber is designed in such a manner that either of the rounded outlets can be installed.

Water discharged from the outlet is channelled through a funnel-diverter system directing the water into either of two separate graduated cylindrical tanks for volume measurement.

A general lay-out of the apparatus is shown in Fig. 19 and Plate 1. This experimental set-up permits the adjustment of the vortex chamber height and the insertion of the exit orifice diameter thereby enabling the effect of the slenderness ratio and radius ratio on the swirl flow to be investigated. In addition, the speed of rotation of the chamber can be controlled while, at the same time, keeping both the top and bottom plates rotating at the same angular velocity. Special design is incorporated in the apparatus to allow dye injection for flow visualization.

5.3 Effect of Radius Ratio

Tests were carried out using two outlets of 0.25 and 0.5 inch diameter. The smooth aluminum top plate is set at a height of 0.25 inch while the water level inside the plexiglass tank is adjusted to maintain a constant pressure head, H, of 9.0 inches. The procedure described previously in Section 4.3 is followed and the resulting discharge coefficient is plotted against the swirl coefficient in Fig. 20. The points at which the air core was first observed at the outlet and the points at which the air core is fully developed are indicated on the figure for the two outlets.

The two curves show the same trend of variation of C_d with X. For each curve, the value of C_d remains constant until an air core is formed at the outlet and then decreases with the increase of X. Since the formation of an air core is more difficult for the case of a small diameter outlet, therefore the first phase of swirling flow occurs over a larger range of swirl for the outlet with smaller diameter. Also, under medium and high swirl conditions, the smaller the outlet diameter, the higher the coefficient of discharge. This is also shown theoretically by eqn. 3.11.

The reverse flow phenomenon starts at X = 0.65 for the small outlet while it does not appear for the large outlet within the tested swirl range. This is because of the limited capacity of the small outlet which cannot handle the increasing boundary-layer flow resulting from increasing swirl.

The discontinuity observed at X = 0.6 on the curve for the smaller outlet in Fig. 20 is found to occur at the point where the air core becomes fully developed. Again, this discontinuity does not appear in Fig. 21 when the test is carried out in the reverse direction beginning with the maximum value of X with the air core fully developed and then decreasing the swirl in steps. This discontinuity is also explained by the sudden change in the shape of the air core as discussed in Section 4.5 for the case of a stationary vortex chamber. The curve for the large outlet in Fig. 20 does not show any discontinuity due to the fact that the air core is more readily formed when the outlet diameter is increased.

5.4 Effect of Slenderness Ratio

The two outlets were then tested with the top aluminum plate set at a height, 2h, equal to 4, 0.5, 0.25, 0.125, 0.0625 and 0.03125 inches. The same procedure was carried out with a constant pressure head of 9.0 inches of water above the outlet. The results for the large radius ratio (R/r = 24.0) of the 0.25 inch diameter outlet are presented in the set of curves in Fig. 22, while the results for the small radius ratio (R/r = 12.0) of the 0.5 inch diameter outlet are presented in Fig. 23.

In general, these results show that at medium swirls the coefficient of discharge decreases as the slenderness ratio increases while there is no appreciable effect at high swirls. This is due to the reduction in the potential flow area inside the chamber at medium swirls. The results indicate that the slenderness ratio has no effect on the growth of the boundary layer which is confirmed by the theoretical solution given in Chapters II and III. At a very large slenderness ratio, the boundary layers may merge inside the chamber and the coefficient of discharge at high and medium swirls increases drastically as shown in Fig. 22 for R/h = 96.0 and 192.0. This may be explained by the fact that when the two boundary layers merge, the tangential velocity decreases and consequently the centrifugal effect is reduced. The results at weak swirl show that the coefficient of discharge decreases at a very large slenderness ratio. This happens when the capacity of the outlet is much larger than the cross-section of the flow area [$2\pi a(2h)$] before entering the outlet orifice.

The points at which the air core is first observed at the outlet and at which the air core is fully developed are given in the following table.

R/a	X	R/h					
		1.5	12	24	48	96	192
24	start of air core at outlet	0.22	0.31	0.32	0.47	0.56	0.59
	start of fully developed air core	0.75	0.67	0.60	0.59	0.78	0.89
12	start of air core at outlet	0.21	0.13	0.12	0.12	0.12	0.12
	start of fully developed air core	0.49	0.41	0.33	0.37	0.55	0.67

The table shows that the air core at the outlet starts at higher values of X as the slenderness ratio increases. The fully developed air core starts at lower values of X as the slenderness ratio increases. When the slenderness ratio reaches a critical value, the trend starts to reverse. It is believed that this critical value of the slenderness ratio is governed by the condition at which the two boundary layers start merging with each other inside the chamber.

5.5 Effect of the Supply Pressure Head

Each of the outlets is tested again at the three slenderness ratios 12, 24 and 96, maintaining two constant pressure heads of 7.0 and 5.0 inches of water. The experimental results for each slenderness ratio are shown in Figs. 24 to 29. For comparison, the results obtained previously in Section 5.4 for the same slenderness ratio, with H = 9 inches of water, are included. In all six sets of curves, it is observed that at medium and high swirls, the effect of pressure head variation on the discharge coefficient is very small.

It is worthwhile to mention that eqn. 3.11, even though approximate, is able to predict these small variations in the coefficient of discharge as shown in Fig. 30 for R/a = 12 and R/h = 12 at H = 5, 7 and 9 inches of water.

It is observed that as the supply pressure head decreases, the first weak swirl phase extends over a greater range. This may be explained by the fact that the pressure gradient for a lower pressure head is less. Eqn. 2.12 indicates that the angular velocity is directly proportional to the square root of the pressure gradient; therefore, the angular velocity at the outlet will be less for the lower supply pressure head. Since the formation of the air core is directly dependent on the magnitude of swirl, then higher swirls will be required to attain an air core as the supply pressure head is reduced.

5.6 Flow Pattern

The flow pattern inside the vortex chamber is examined by injecting coloured phospheric dye by means of an L-shaped tube, as shown in Fig. 18. This tube can be located very close to the radial vanes at different levels inside the tank. The photographic arrangement used is shown in Fig. 31. These examinations of the flow pattern are carried out for each outlet at various degrees of swirl with the top plate set at a height of 4 inches, i.e., R/h = 1.5. It is anticipated that there is visual distortion of the flow pattern resulting from both the different refractive index of the liquid and from the cylindrical configuration of the apparatus. However, this flow visualization technique is only used to obtain qualitative results of the actual flow pattern, therefore no correction is included.

At zero swirl, the pattern was simple and the streamlines converged from all points towards the outlet. At the first phase of weak swirl, the dye injected at different levels showed helical streamlines converging from all points towards the outlet. This confirms the physical model described previously: that at low swirl, the flow configuration is very similar to that of the pure radial flow while inward radial flow component exists at all points within the chamber.

As the second phase is reached, a small part of the dye injected near the top plate moves inward into the boundary-layer flow and then downward to the outlet through the core. This core flow is very small during this second phase of critical swirl and sometimes does not appear at all because of the unsteady condition of the flow during this phase. This unsteady phenomenon, as explained earlier, is due to the abrupt change of discharge coefficient resulting from the formation of the air core.

When the air core establishes itself at the outlet during the third phase, termed medium swirl, the core flow is clearly visible and steady as shown in Plate 3 for the 0.25 inch diameter outlet at $X = 0.5$. The dye injected near the bottom moves inward through the bottom boundary-layer current and is discharged directly through the outlet. The dye injected at intermediate levels of the vortex chamber does not show any definite pattern but when the injection is stopped the dye is eventually washed away indicating that part of the outlet flow is being fed by the potential flow as well.

At the last stages of medium swirl, i.e. $X \approx 1$, when the dye is injected near the bottom of the chamber with 0.25 inch diameter outlet, a part of the bottom boundary-layer flow separates and moves upward around the core flow showing the existence of reverse flow as shown in Plate 4 for $X = 0.7$. This reverse flow does not appear clearly for the large outlet within the range of swirl tested. This phenomenon was explained in Section 4.7, i.e. the flow capacity of the 0.5 inch diameter outlet is more than adequate to drain the flow within the range of swirls tested and, consequently, no severe pressure builds up in the vicinity of the exit.

Injection of dye into the potential flow region during the phase of high swirl shows no definite pattern and when the injection is stopped, the dye remains. This strongly suggests that the potential flow does not feed the outlet. When the air core is fully developed, the core flow surrounds the air core, as shown in Plate 5 for the 0.25 inch diameter outlet at X = 1.8, and in Plate 6 for the 0.5 inch diameter outlet at X = 0.75.

To demonstrate the shapes of the air cores inside the chamber, Plates 7 and 8 are presented for R/a = 12 and R/h = 1.5. Plate 7 shows the air core on its way up at X = 0.5, while Plate 8 shows the air core after reaching the top plate at the same value of X.

5.7 Velocity Measurements

The technique of the two immiscible liquids used in Section 4.8 for measuring the core flow is used to measure the radial velocity distribution inside the vortex chamber at the outlet radius. At any constant swirl, if the depth of kerosene above the water inside the vortex chamber is maintained constant at z, a constant flow rate of kerosene, Q_K, can be obtained at the outlet. Similarly, when the depth of kerosene above the water is maintained constant at $(z + \Delta z)$, the constant volume flow rate of kerosene at the outlet will be $Q_K + \Delta Q_K$. Then the mean radial velocity through the layer Δz at the outlet radius will be:

$$U_m = \frac{\Delta Q_K}{2 \pi a \Delta z} \qquad (5.1)$$

In the tests, the step size Δz is chosen to be constant and equal to 0.25 inch. The mean velocity U_m can be determined by measuring ΔQ for each increment Δz.

In order to apply this technique to the apparatus, kerosene is supplied under gravity from an elevated tank through a regulating valve. It is important that an oil trap be used during this procedure for safety reasons. The oil trap used in this investigation consists of two tanks in series with the general arrangement shown in Fig. 32.

The results of the radial velocity distribution at the outlet radius for the 0.25 inch outlet with 4.0 inches vortex chamber height are presented in Figs. 33 and 34 for $X = 1.0$ and $X = 1.5$, respectively. These results show that the radial velocity is maximum near the boundaries and is almost zero at the intermediate region of the chamber. This agrees with the assumptions used in achieving the theoretical solution for the high swirl case. Also, it is worth mentioning that the radial velocity distributions obtained are very similar to those in reference (23) using a pitot tube, and in reference (28) using a hot-wire anemometer.

Plate 13 demonstrates the case where kerosene is supplied above the water with the kerosene core flowing directly towards the outlet.

A comparison of the experimental results for the core flow of kerosene and the theoretical calculations using eqn. 3.7, at $X = 1.5$ and $X = 1.0$, shows that they differ by a minimum and maximum of 2-10% respectively.

5.8 Comparison Between Theory and Experimental Results

Eqn. 3.16 of Chapter III for the coefficient of discharge through rotating vortex chambers is now applied to the vortex chamber described in Section 5.2. The parameters substituted in these equations are:

$\nu = 10.9 \times 10^{-6}$ ft^2/sec

$H = 0.75$ ft

$a = 0.25$ inch

$R = 0.25$ ft

$\xi_a = (a/R) =$ 1/12

$g = 32.2$ ft^2/sec

and the coefficient of discharge, C_d, is then calculated for different values of ω. The results are presented in Fig. 35 together with the experimental results for the two non-dimensional quantities C_d and X. Again, the theory shows that at medium swirls, the discharge coefficient decreases as the swirl increases until $X = 1$, at which point the potential flow ceases to feed the outlet.

It should be noted that the correspondence between theory and experimental results is very good because the experimental apparatus permits investigation of a much larger slenderness ratio. This close correspondence further substantiates the argument given in Section 4.9.

Again, at high swirl, the theory predicts a slight increase in discharge coefficient. This behaviour was explained previously as being due to the secondary effect of high swirl on the fully developed air core which was not considered in the analysis.

The boundary-layer thickness, δ , which was calculated based on experimental data, is again used to compare the theoretically predicted boundary-layer profile. Two sets of experimental results for the 0.25 and 0.5 inch diameter outlets at X = 1 are used and the experimental values are shown in Fig. 36 together with the theoretical profile.

In general, both the theoretical curves and experimental data exhibit a similar trend with a maximum difference of less than 20%. However, the difference is much reduced near the outlet region which is of great importance in predicting discharge coefficients for practical applications.

CHAPTER VI

CONCLUSIONS AND RECOMMENDATIONS FOR FURTHER WORK

6.1 Conclusions

The swirling flow of liquids within stationary and rotating cylindrical chambers has been investigated both analytically and experimentally. This is an attempt to classify the vortex flow of liquids to the atmosphere into four well-defined flow regimes. These flow regimes covered the range from zero swirl (i.e. $X = 0$) to high swirl (i.e. $X \geqslant 1.0$), where X is a dimensionless swirl coefficient equal to $\Omega/a\sqrt{2gH}$.

The theoretical phase of the investigation was concerned with the development of analytical solutions of the boundary-layer momentum integral equations applied to confined vortex flow. Explicit relationships for the discharge coefficient as a function of the physical and geometrical parameters for both types of swirl chambers were obtained at medium and high swirl conditions. For weak swirls, it was verified experimentally that the discharge coefficient is identical with that of pure radial flow.

The experimental investigations covered a wide range of swirl conditions and various boundary conditions. Also, a unique method using two immiscible liquids was used to measure the core flow and the radial velocity distribution without disturbing the nature of the flow. Flow visualization techniques were used to confirm the validity of the assumptions used in the theoretical analysis.

Generally good agreement between the theoretical and experimental results was achieved. Also, the theory gives good prediction of the discharge coefficient through vortex chambers at medium and high swirls, thus providing useful information, especially for engineering purposes.

6.2 Recommendations for Further Work

The experiments in flow visualization show that for very large radius ratios, when the outlet diameter is very small, throttling effects create a back-pressure which helps the boundary layer to separate demonstrating what is termed "reverse flow". The obvious extension of the present theoretical work would be study the above-mentioned phenomenon. This could be established by careful theoretical and experimental work in which measurements of the pressure distribution inside the vortex chamber would be carried out.

REFERENCES

1. Posey, C.G. How the Vortex Affects Orifice Discharge. Engineering News-Record, March 9, 1950, p. 30.
2. Crump, E.S. A Vortex-Siphon Spillway for Maintaining a Constant Water Level Upstream of a Structure. Inst. of Civil Engineers, Paper No. 6032, Part 3, 1955, p. 139.
3. Kolf, R.C. Vortex Flow Through Horizontal Orifices. A.S.C.E. Transactions, Vol. 124, Paper No. 3004, 1959, p. 871.
4. Kamel, M.Y. The Effect of Swirl on the Flow of Liquids Through Bottom Outlets. A.S.M.E. Publications, Paper No. 64-WA/FE-37, 1964.
5. Anwar, H.O. Flow in a Free Vortex. Proc., Water Power, April, 1965, p. 153.
6. Gartshore, I.S. Recent Work in Swirling Incompressible Flow. National Research Council of Canada, Aeronautical Report LR-343, 1962.
7. Gartshore, I.S. Some Swirling Flow Phenomena and Applications. National Research Council of Canada. PME/NAE Quarterly Bulletin No. 1962(2), July 1962.
8. Donaldson, C. du P. and Sullivan, R.D. Examination of the Solutions of the Navier-Stokes Equations for a Class of Three-Dimensional Vortices. Aero Research Associates of Princeton, AFOSR, TN 60-1277, Oct. 1960.
9. Farag, E.A. The Swirling Flow of Liquids. M.Sc. Thesis, Faculty of Engineering, Cairo University, Egypt, 1969.
10. Taylor, G.I. Mechanics of Swirl Atomizers. Proc. 7th Inst. Can. Applied Mech., Vol. 2, 1948, p. 280.
11. Taylor, G.I. The Boundary Layer in the Converging Nozzle of a Swirl Atomizer. Quart. J. Mech. and Applied Math., Vol. 3, 1950, p. 129.
12. Weber, H.E. Boundary Layer Inside Conical Surfaces due to Swirl. J. of Applied Mechanics, Vol. 23, 1956, p. 587.
13. Wormley, D.N. An Analytical Model for the Incompressible Flow in Short Vortex Chambers. Trans. A.S.M.E., J. Basic Engineering, Paper No. 68-WA/FE-17, 1968.

14. Kwok, C.K. Vortex Flow in a Thin Cylindrical Chamber. Ph.D. Thesis, McGill University, MOntreal, 1966.

15. Einstein, H.A. Steady Vortex Flow in a Real Fluid. La Houille Blanche, Vol. 10, No. 4, 1955, p. 483.

16. Harris, D.P. Swirling Flow Through a Nozzle. M.Sc. Thesis, Engineering Laboratory, Cambridge University, 1949.

17. Ter Linden, A.J. Investigation into Cyclone Dust Collectors. Proc. Inst. Mech. Eng., Vol. 160, 1949, p. 233.

18. Binnie, A.M. and Harris, D.P. The Application of Boundary-Layer Theory to the Swirling Liquid Flow Through a Nozzle. Quart. J. Mech. and Applied Math., Vol. 3, 1950, p. 89.

19. Kamel, M.Y. Swirling Flow of Liquids Through Pipes and Nozzles. Ph.D. Thesis, Engineering Laboratory, Cambridge, 1958.

20. Ashikian, B. The Application of Swirling Water to Obtain a Low Pressure Core. Master's Thesis, McGill University, Montreal, 1962.

21. Donaldson, C. du P. Experimental Investigation of the Structure of Vortices in Simple Cylindrical Vortex Chambers. A.R.A.P. Report No. 47, 1962.

22. Seddon, A.E. and Anwar, H.O. Measuring Fluid Velocities Optically, Engineering, September 1963.

23. Savino, J.M. Experimental Profiles of Velocity Components and Radial Pressure Distribution in a Vortex Contained in a Short Cylindrical Chamber. N.A.S.A. TN D-3072, 1965.

24. Sarpkaya, T. A Theoretical and Experimental Investigation of the Vortex Sink Angular Rate Sensor. Paper presented at the 3rd Fluid Amplification Symposium, 1965.

25. Sarpkaya, T. A Theoretical and Experimental Study of Vortex Rate Gyro. Advances in Fluidics, A.S.M.E., 1967.

26. Neradka, V.F. The Effect of Secondary Vorticity on Vortex Rate Sensors. M.Sc. Thesis, University of Maryland, 1969.

27. Rakowsky, E.I. Fluid Vortex Phenomena in Fluidid Applications. General Precision Aerospace, Technical News Bulletin, Vol. 9, No. 4, 1966.

28. De Santis, M.J. An Experimental Investigation of the Viscous Flow Field in a Pneumatic Vortex Rate Sensor. A.S.M.E. Publications 70, Fluidics 16, 1970.

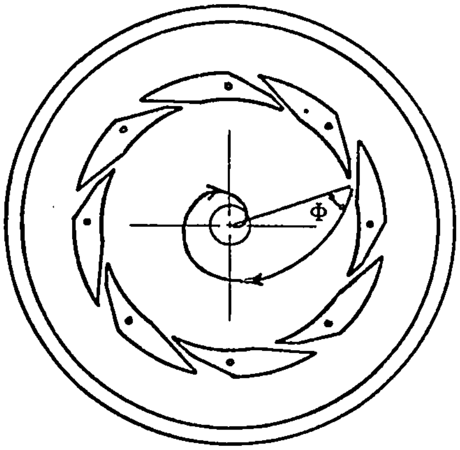

(a) stationary vortex chamber

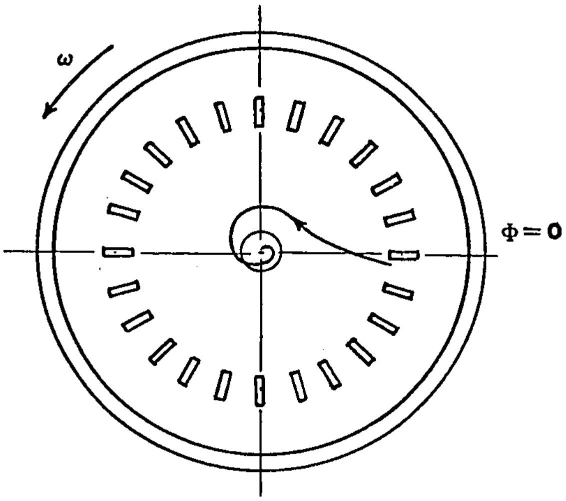

(b) rotating vortex chamber

FIGURE 1 Vortex chamber configurations

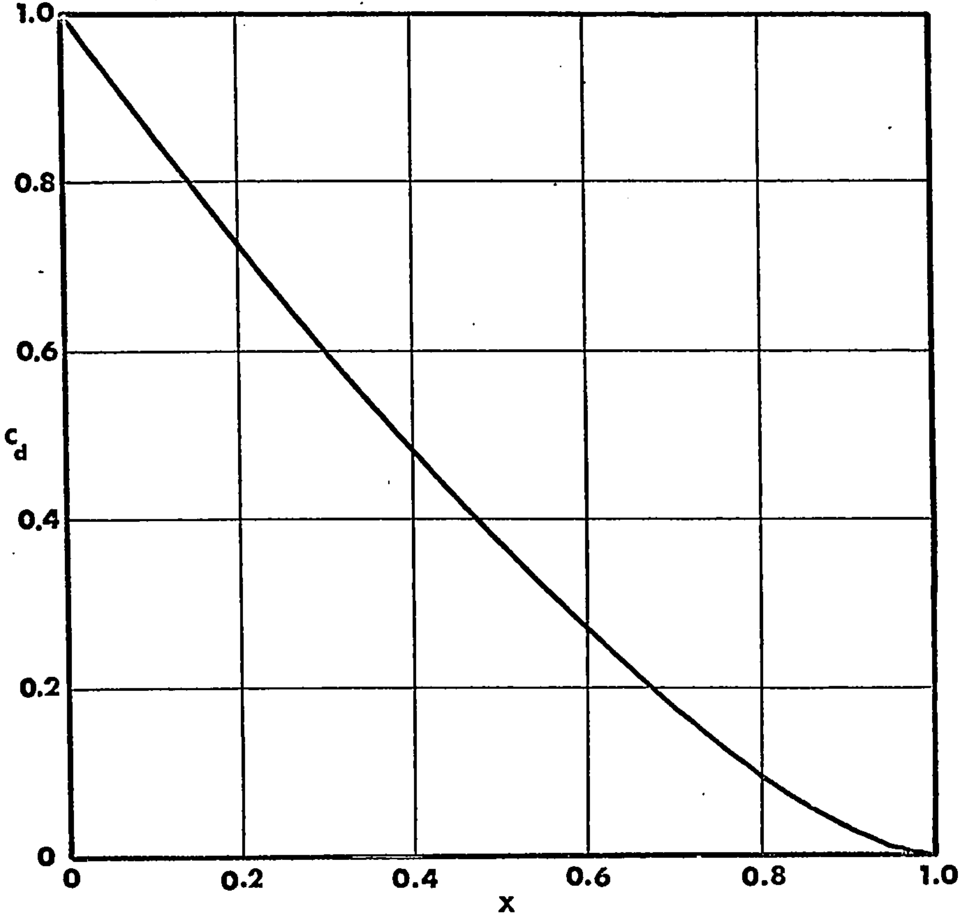

FIGURE 2 Variation of discharge coefficient with swirl coefficient calculated based on the inviscid theory of Taylor (10)

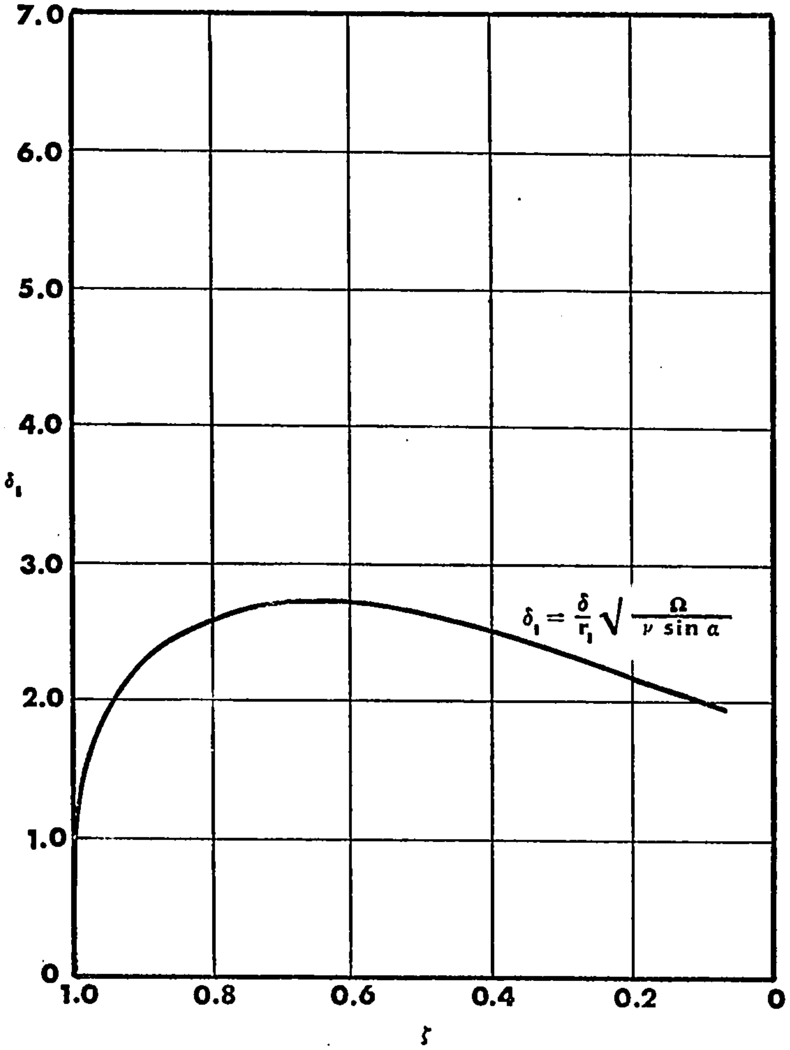

FIGURE 3 Boundary-layer thickness by Taylor (11)

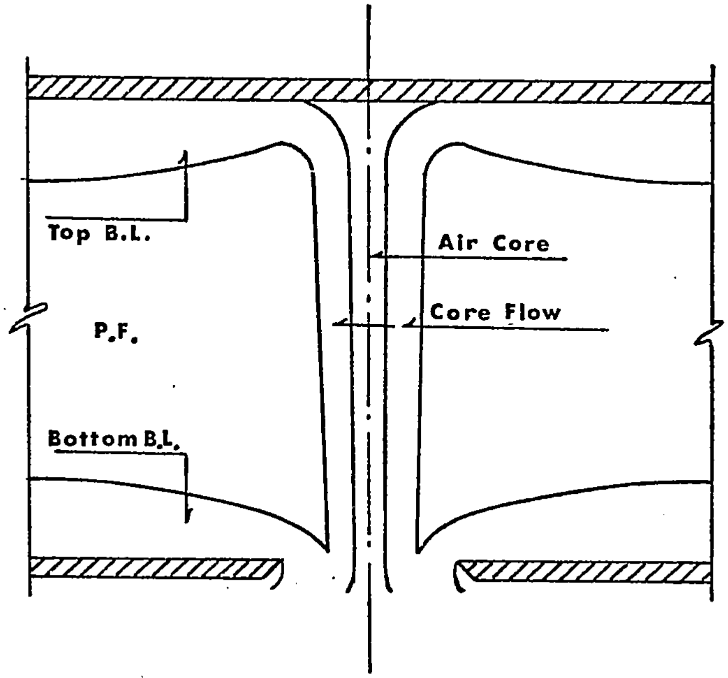

FIGURE 4 Flow configurations at high swirl conditions

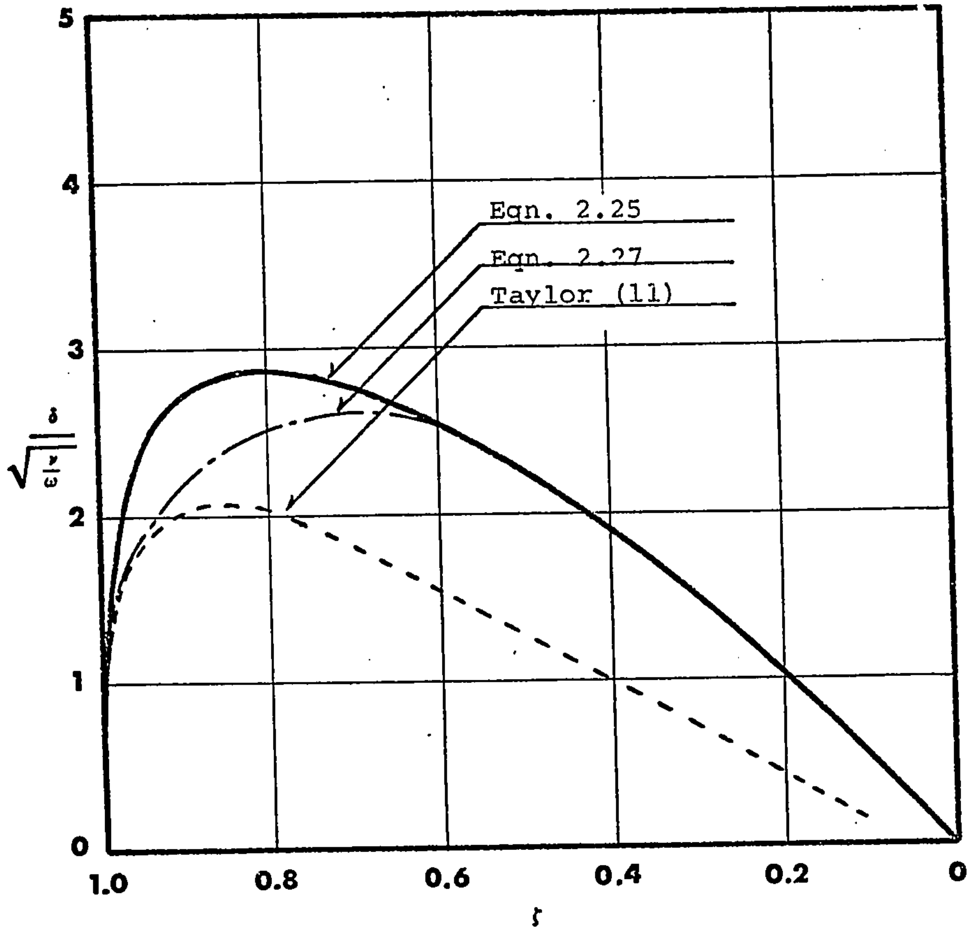

FIGURE 5 Boundary-layer thickness for stationary vortex chambers

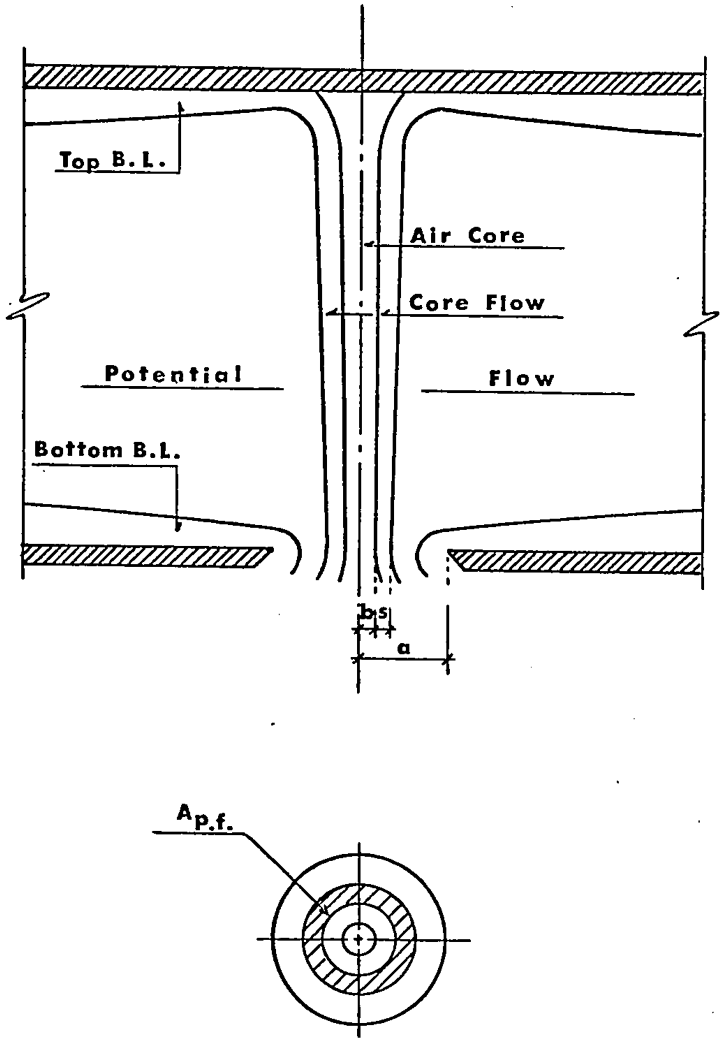

FIGURE 6 Flow configurations at medium swirl conditions

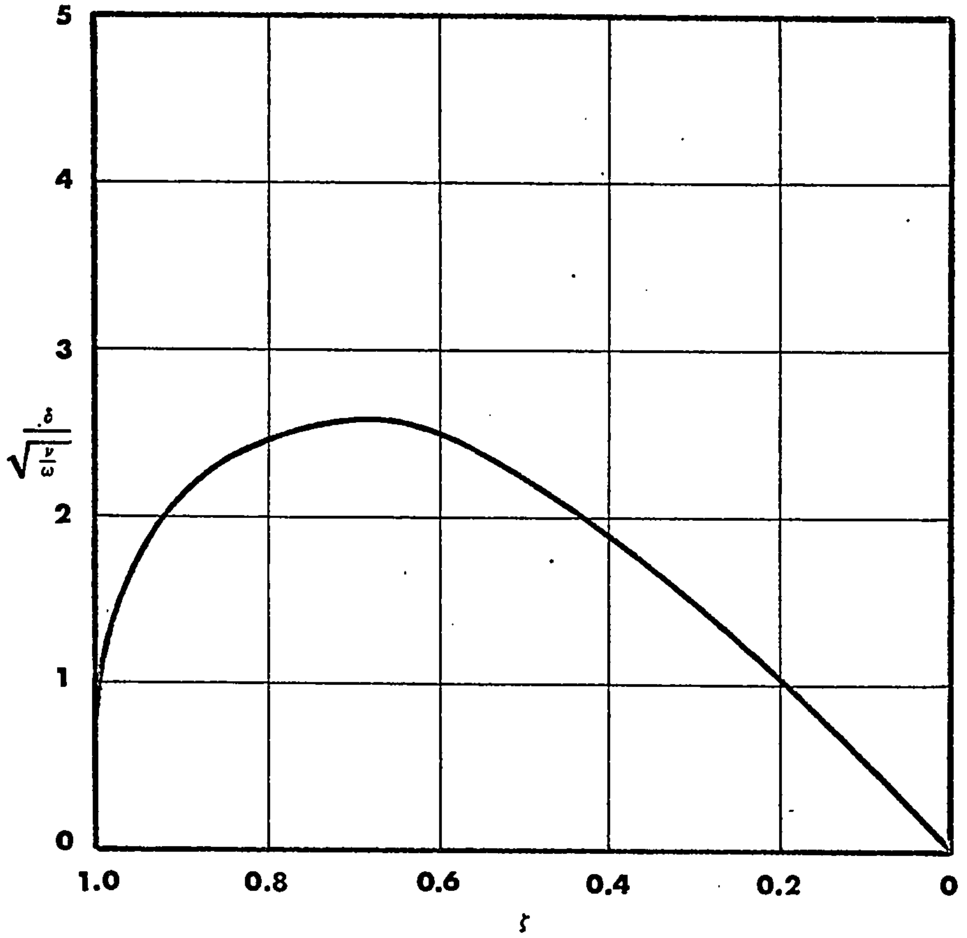

FIGURE 7 Boundary-layer thickness for rotating vortex chambers

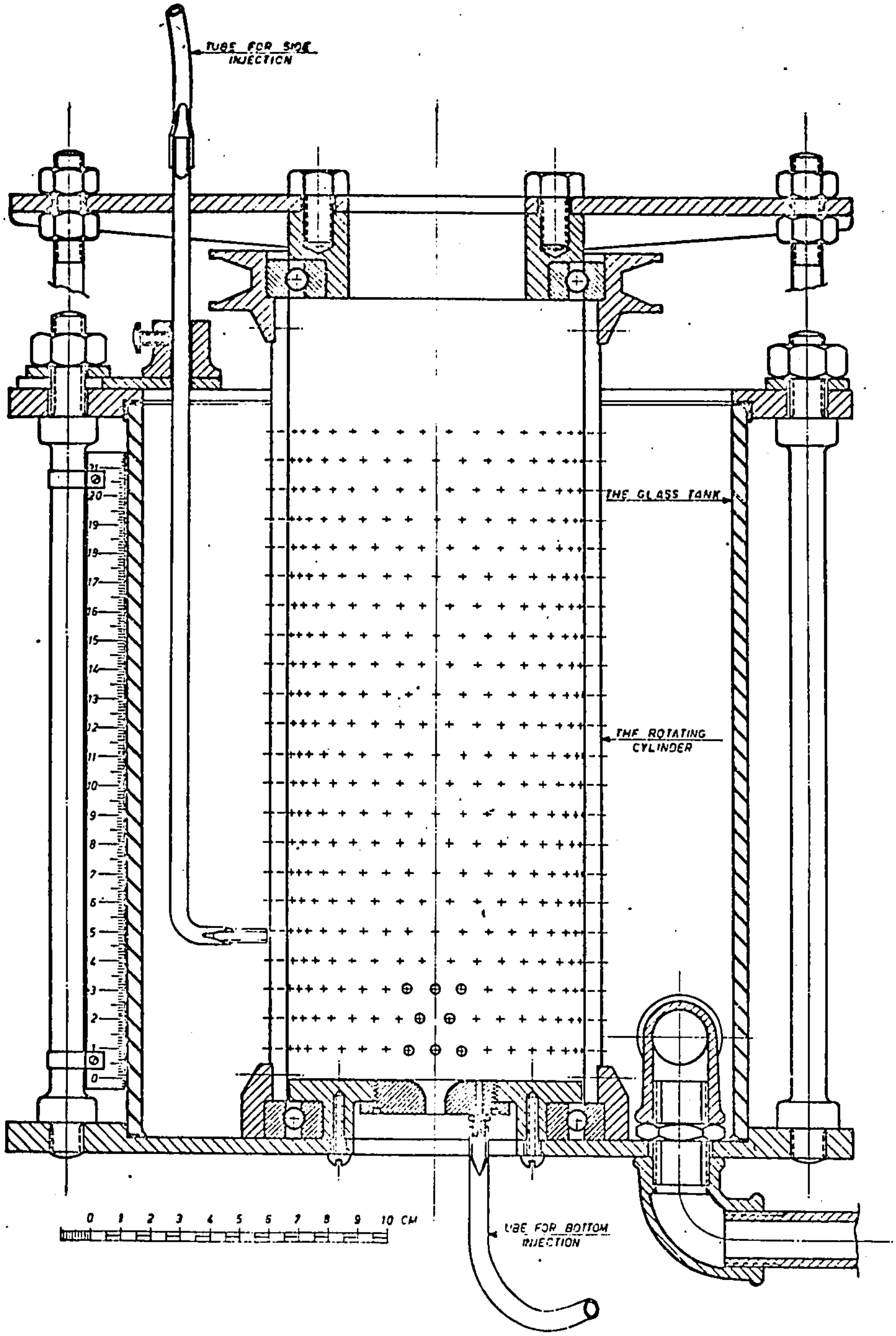

FIGURE 8 Stationary vortex chamber apparatus

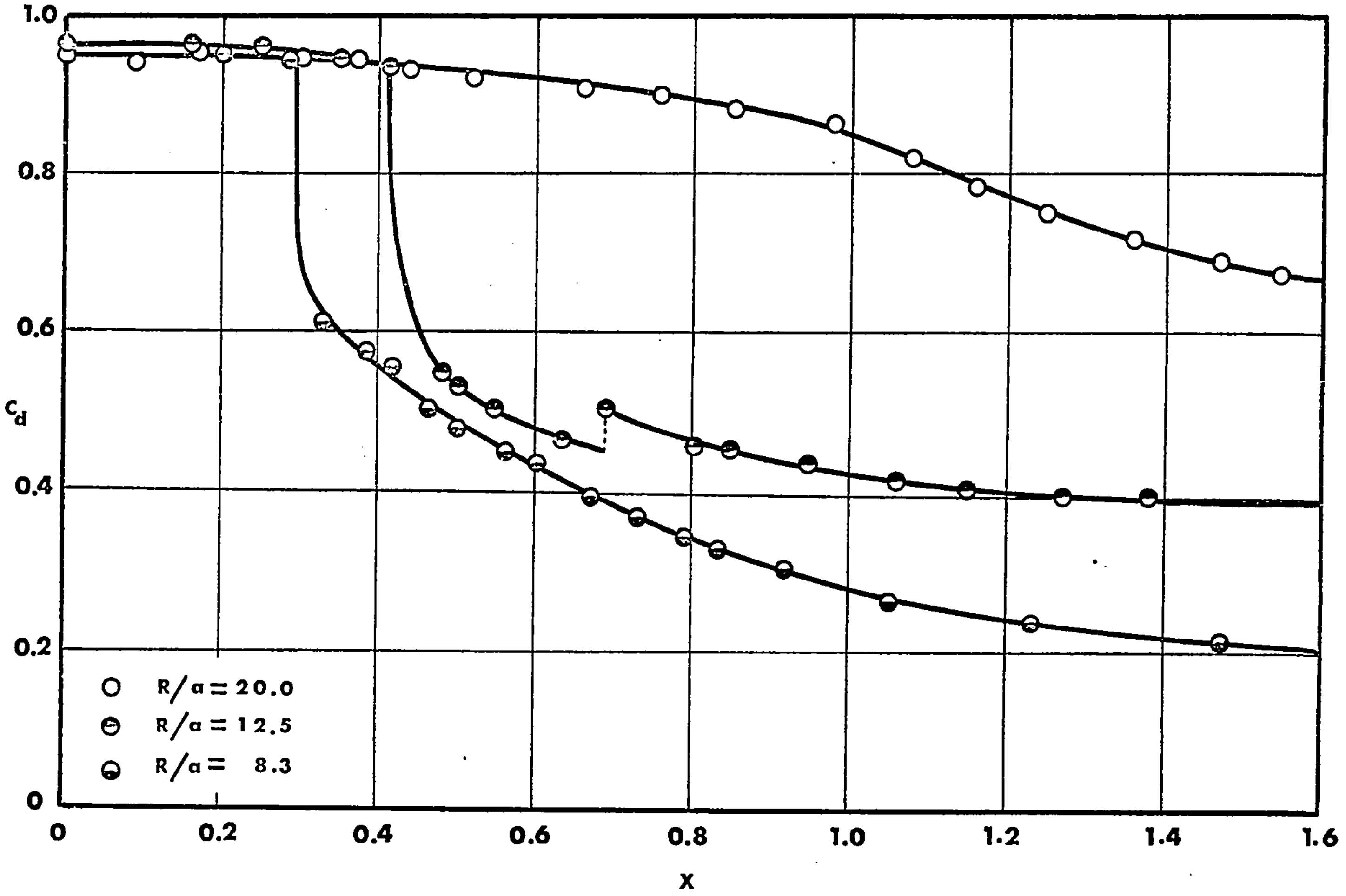

FIGURE 9 Variation of discharge coefficient with radius ratio for stationary vortex chamber

(R/h = 0.59)

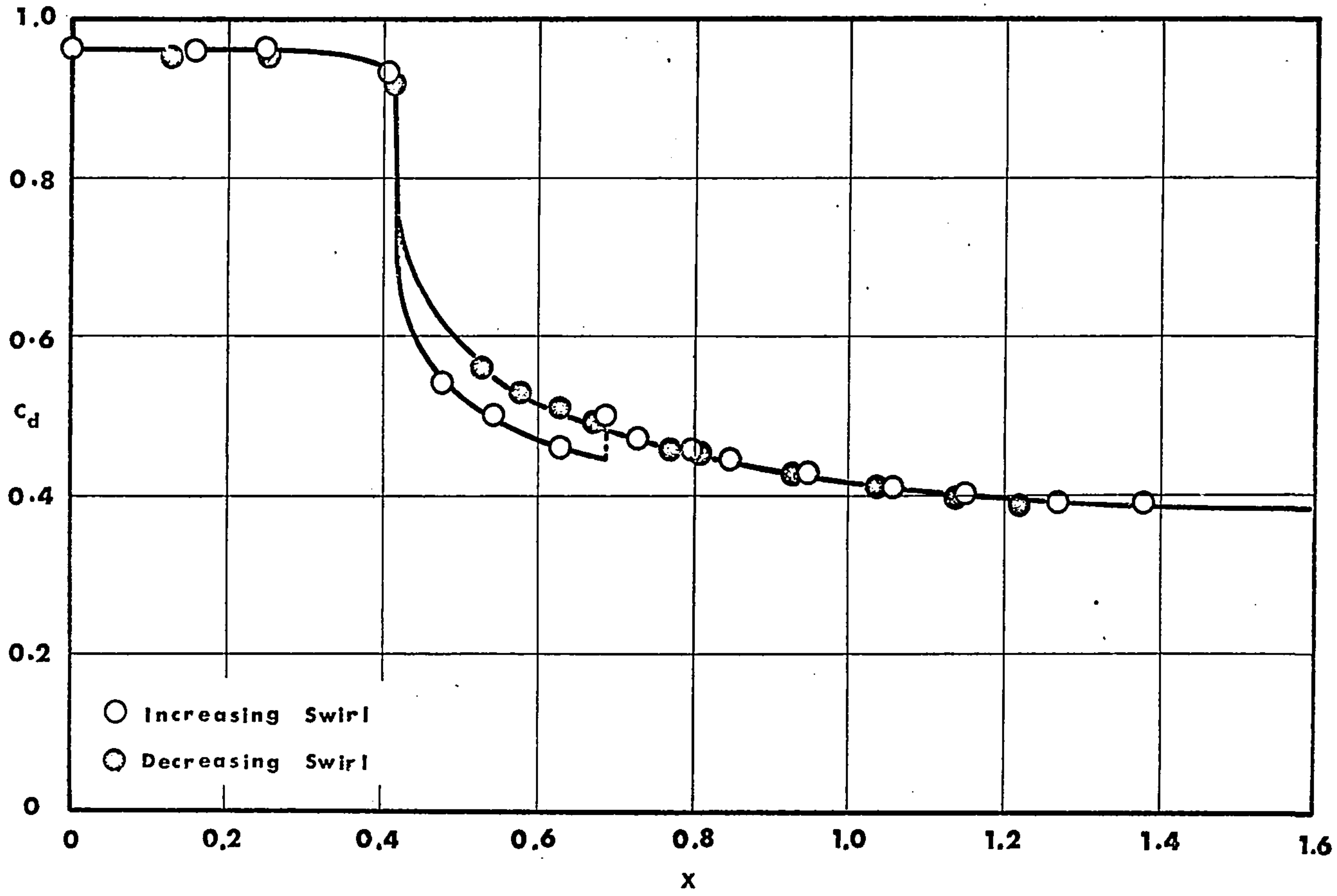

FIGURE 10 Variation of discharge coefficient for increasing and decreasing swirl

(R/h = 0.59, R/a = 12.5)

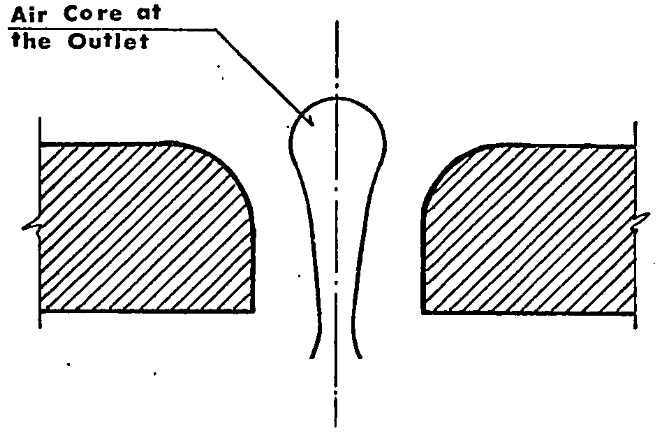

(a) air core at the outlet

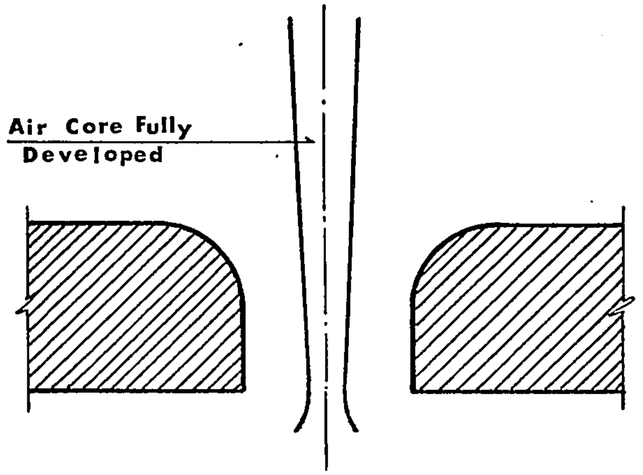

(b) air core fully developed

FIGURE 11 Air core configurations

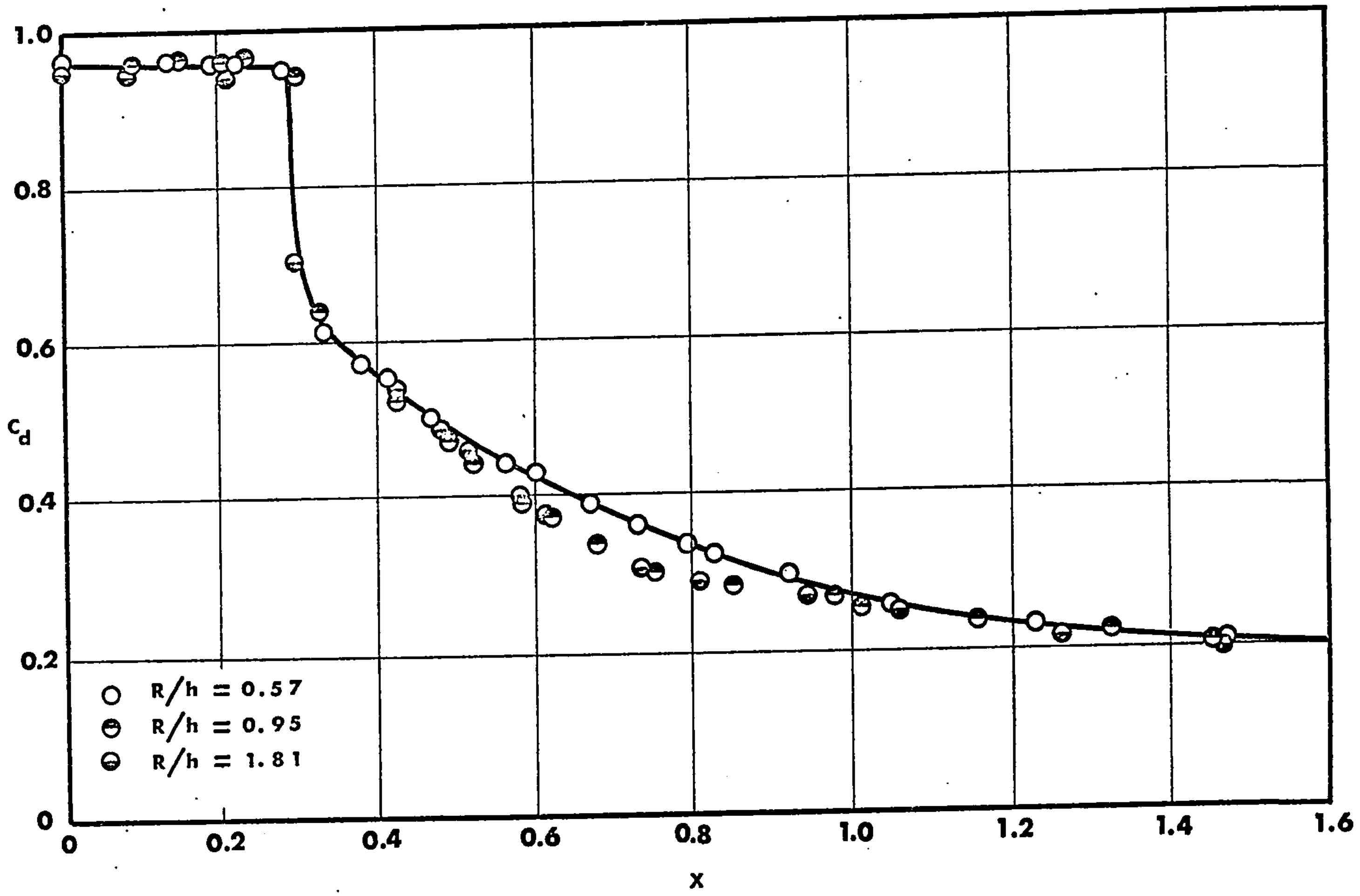

FIGURE 12 Variation of discharge coefficient with slenderness ratio for stationary vortex chamber

(R/h = 8.3)

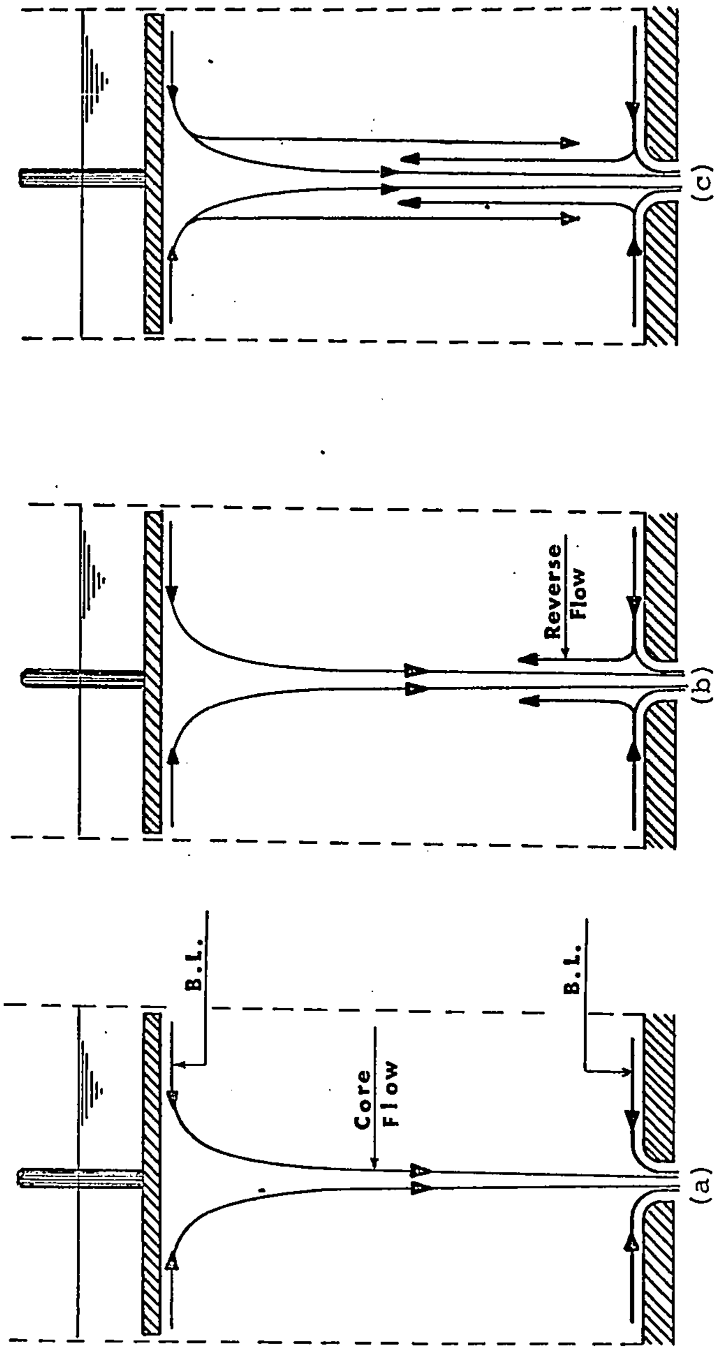

FIGURE 13 Diagrammatic sketch of flow pattern

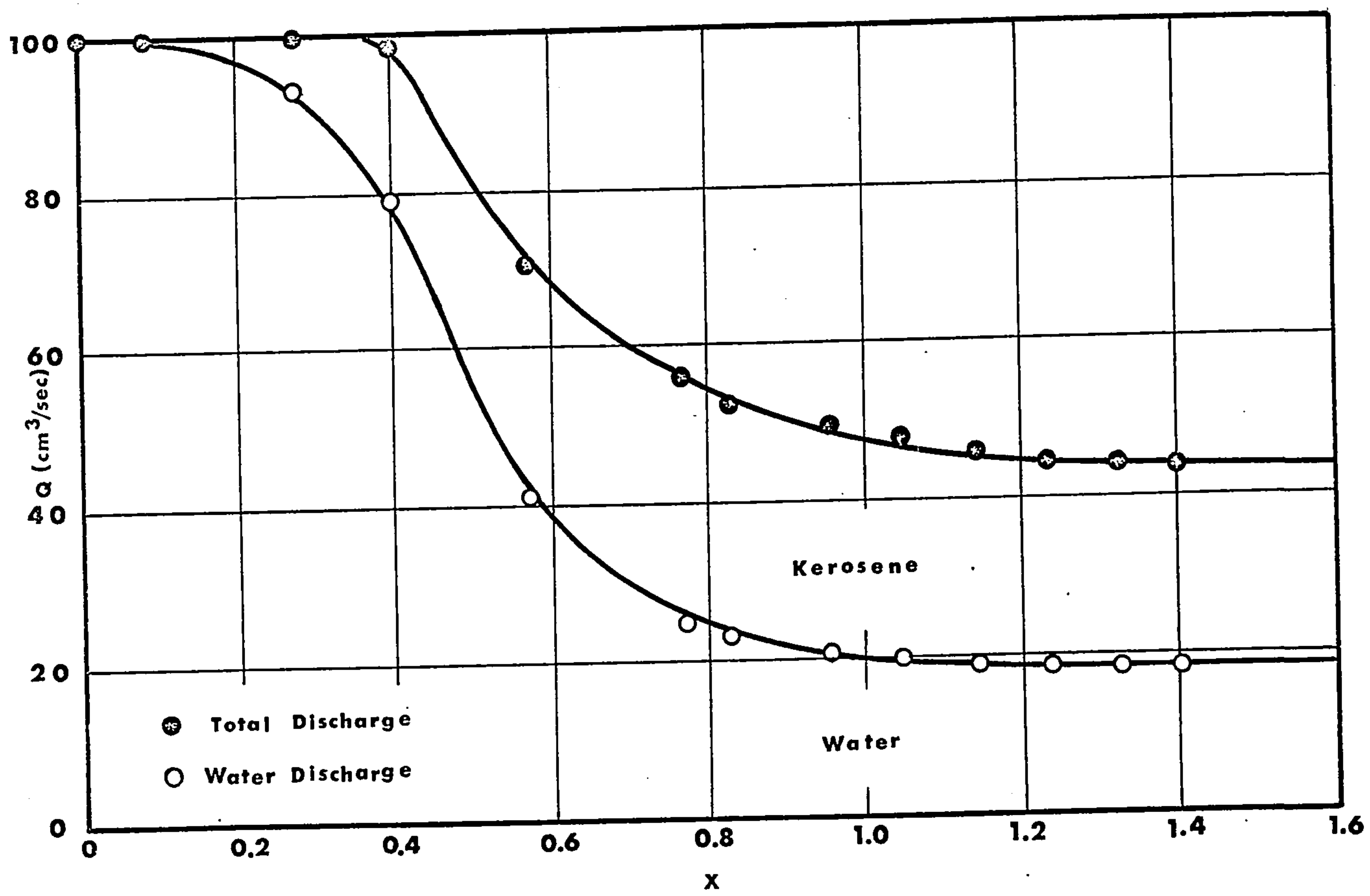

FIGURE 14 Two-liquid flow

(R/a = 12.5, R/h = 0.59)

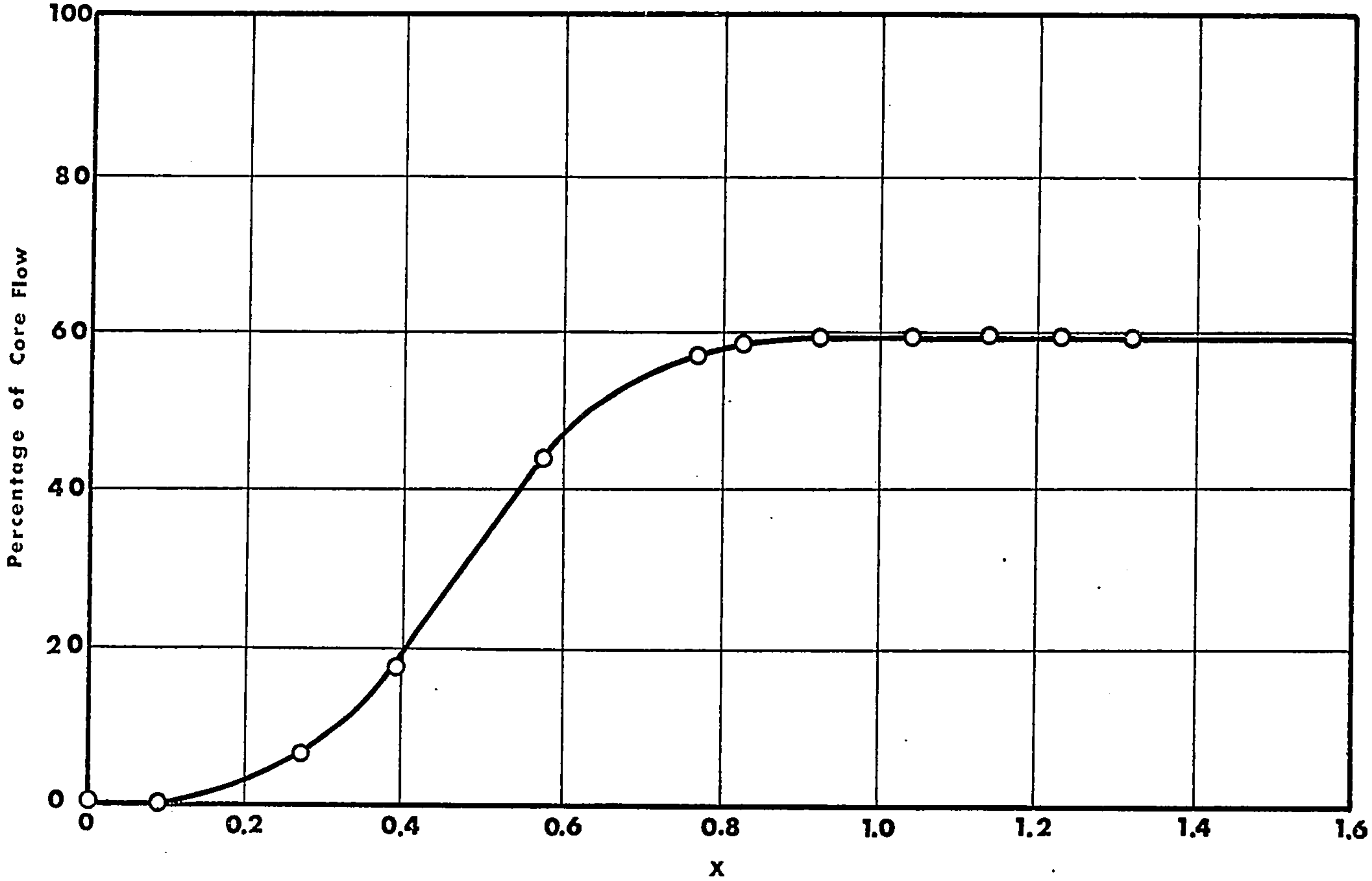

FIGURE 15 Percentage of core flow in the total outflow

(R/a = 12.5, R/h = 0.59)

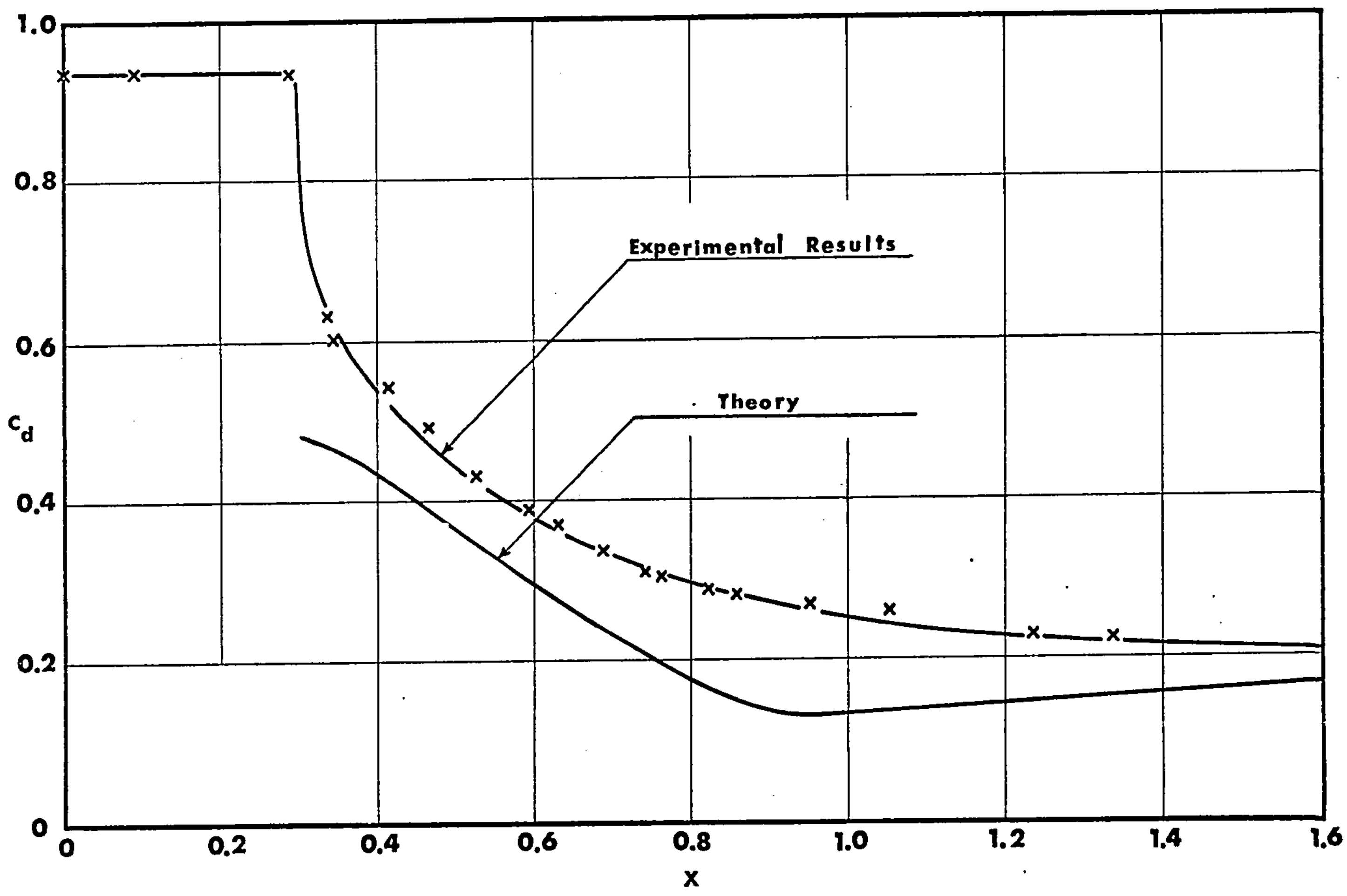

FIGURE 16 Comparison between theory and experimental results for stationary vortex chamber

(R/a = 8.3, R/h = 1.81)

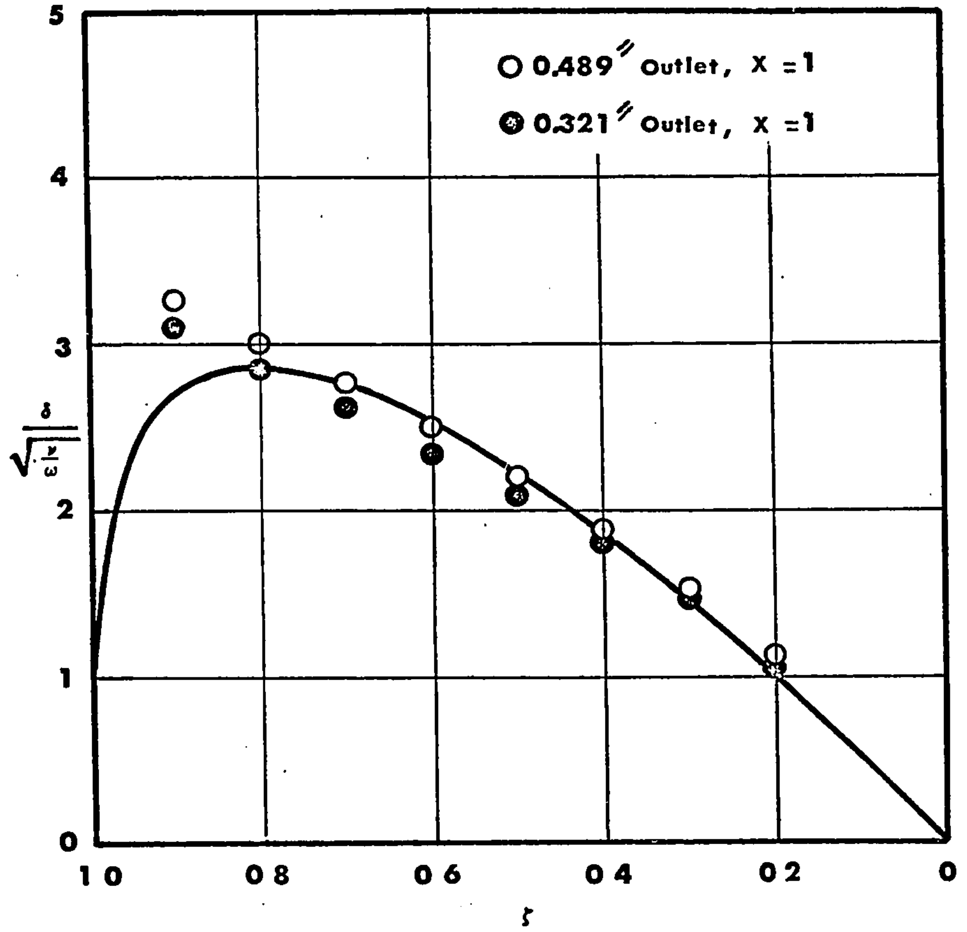

FIGURE 17 Comparison between theoretical and experimental boundary-layer profiles for stationary vortex chamber.

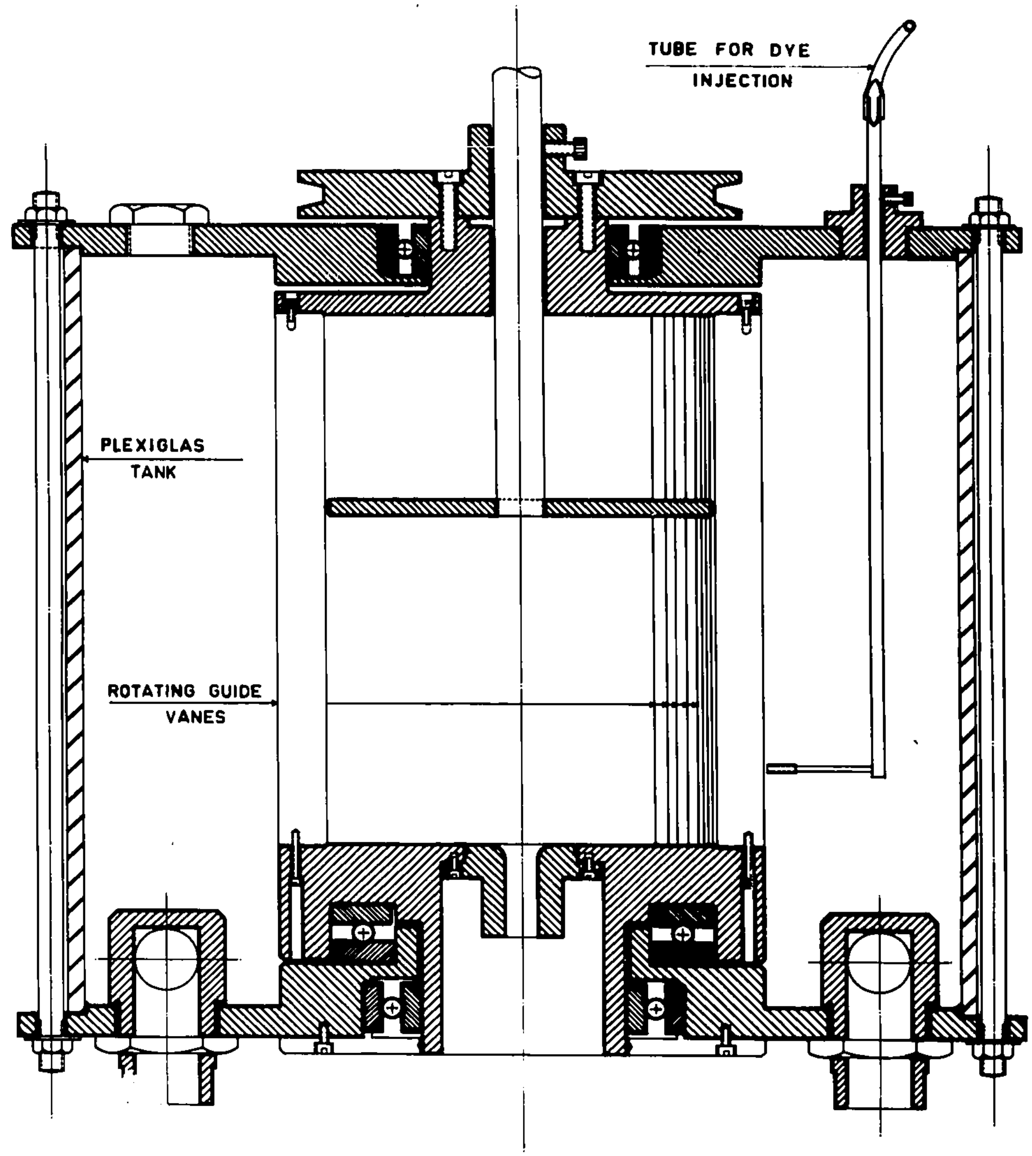

FIG. 18 ROTATING VORTEX CHAMBER APPARATUS.

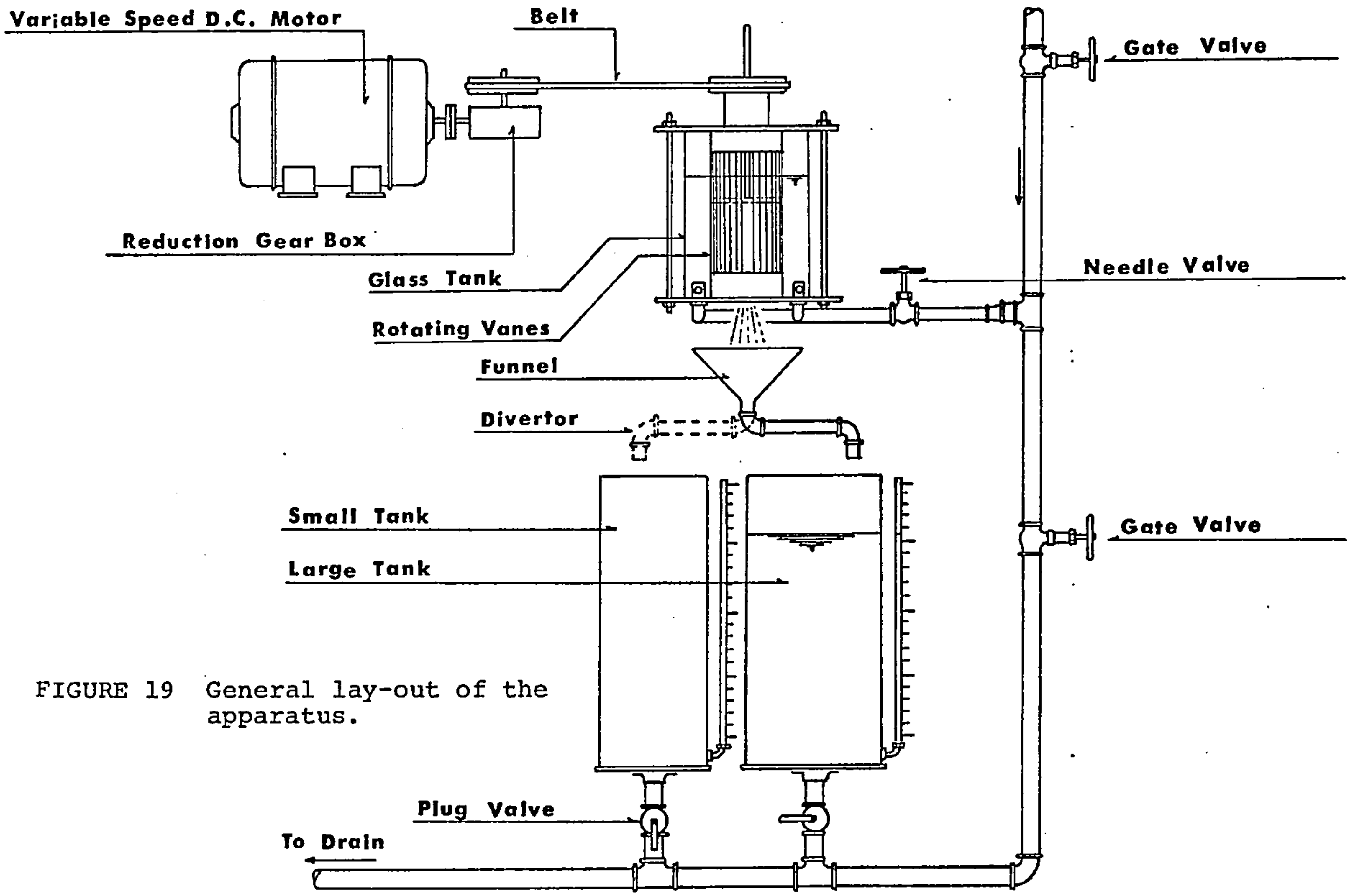

FIGURE 19 General lay-out of the apparatus.

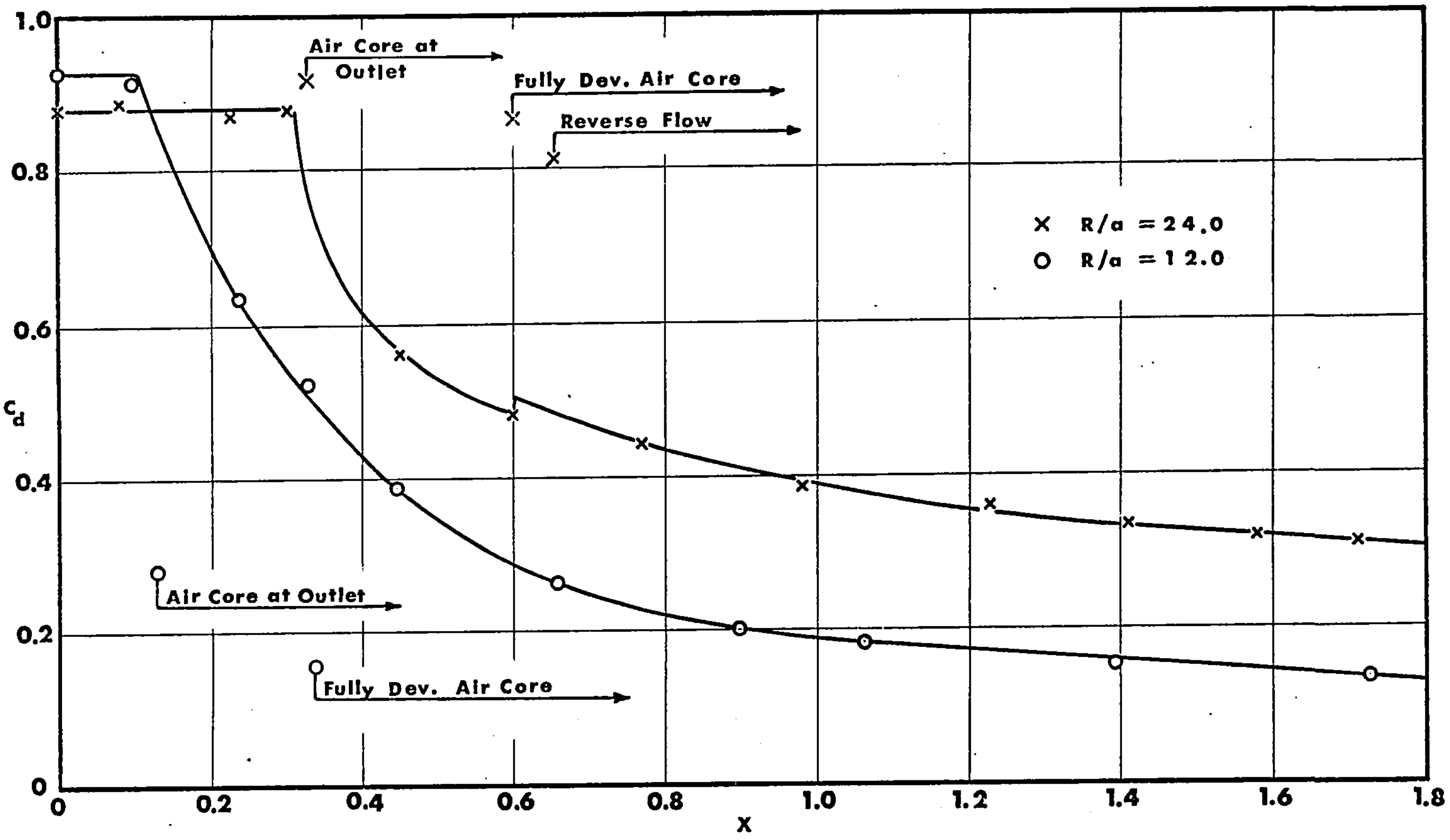

FIGURE 20 Variation of discharge coefficient with radius ratio for rotating vortex chamber

(R/h = 24)

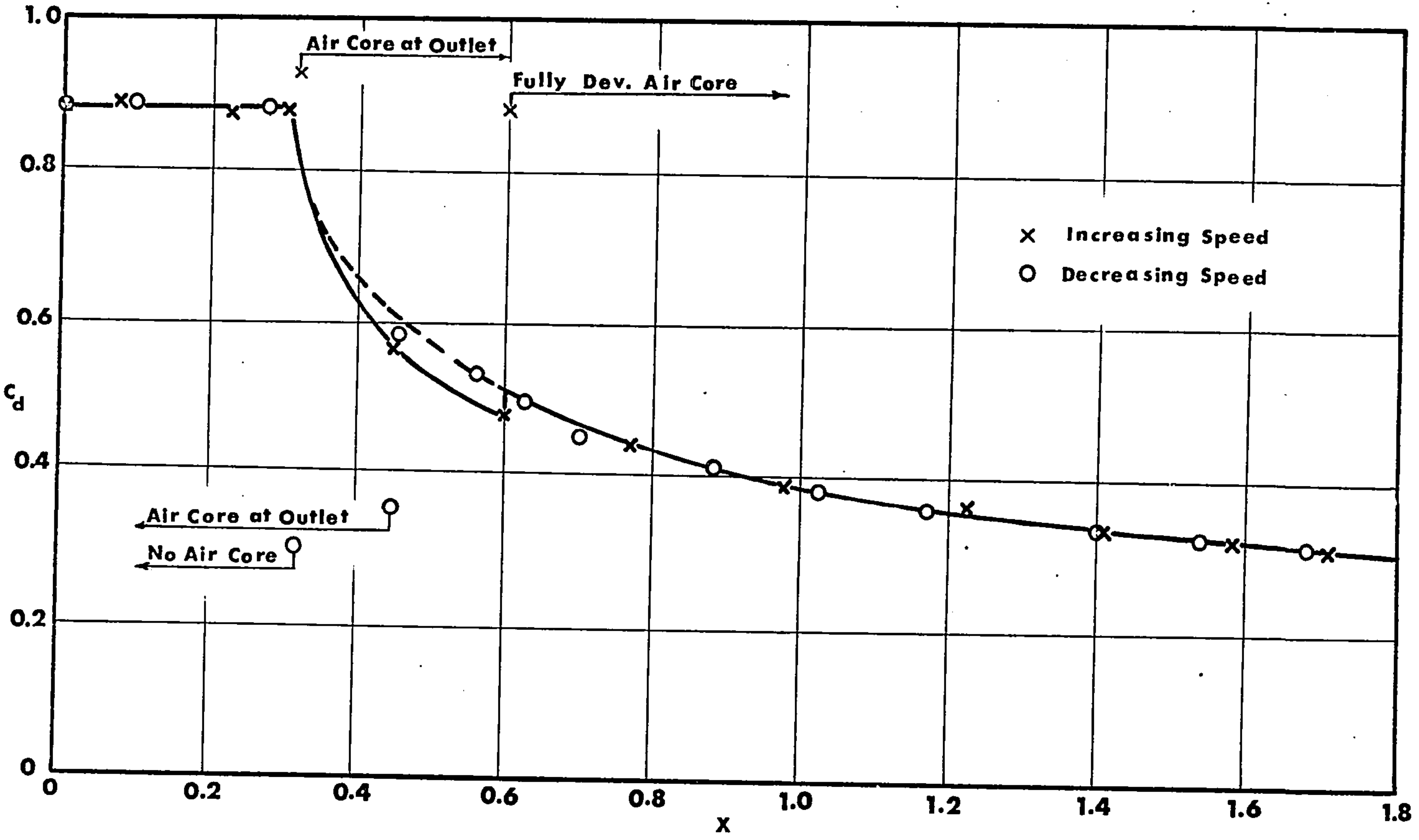

FIGURE 21 Variation of discharge coefficient for increasing and decreasing swirl

(R/a = 24.0, R/h = 24.0)

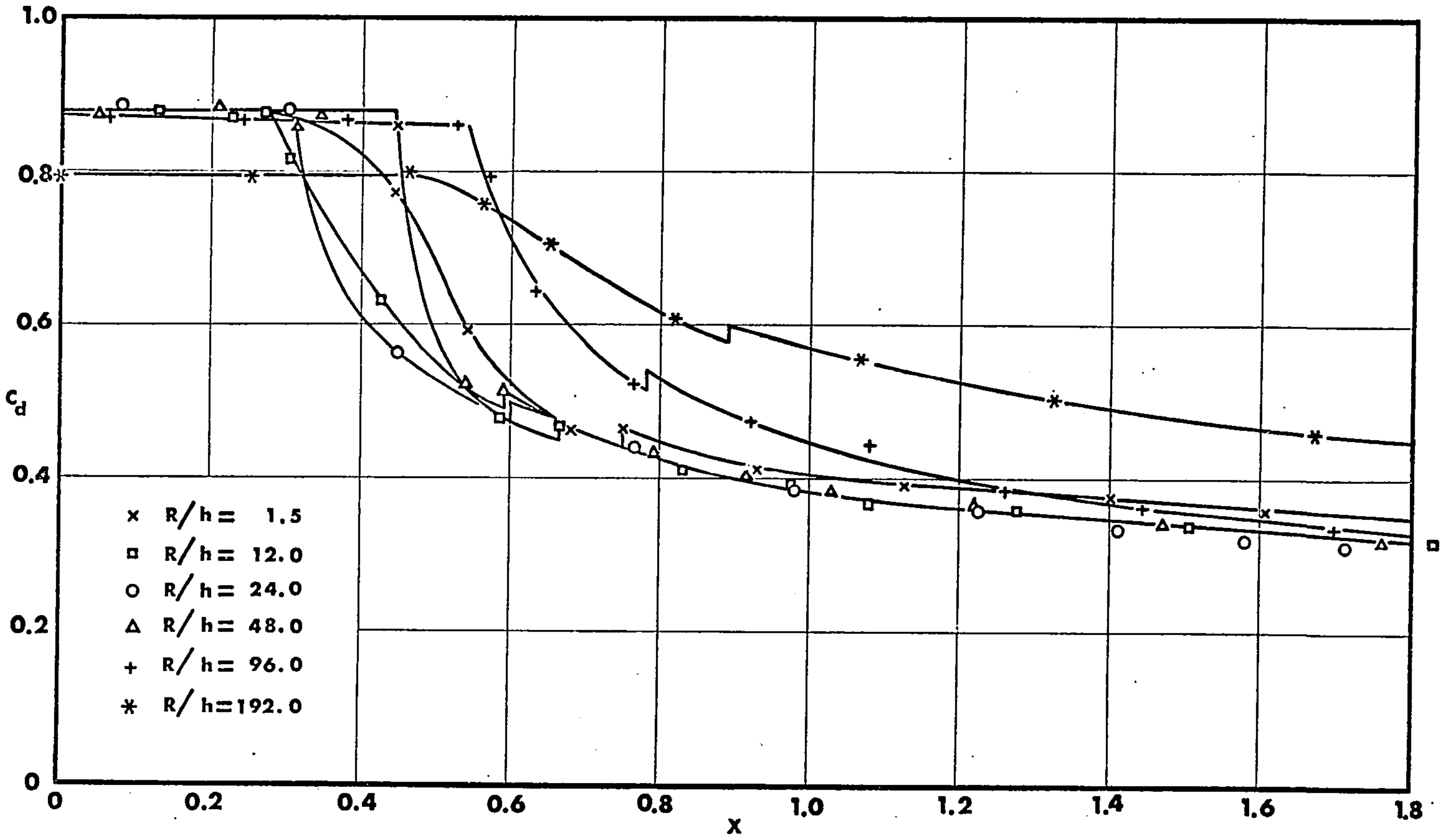

FIGURE 22 Variation of discharge coefficient with slenderness ratio for rotating vortex chamber

(R/a = 24.0)

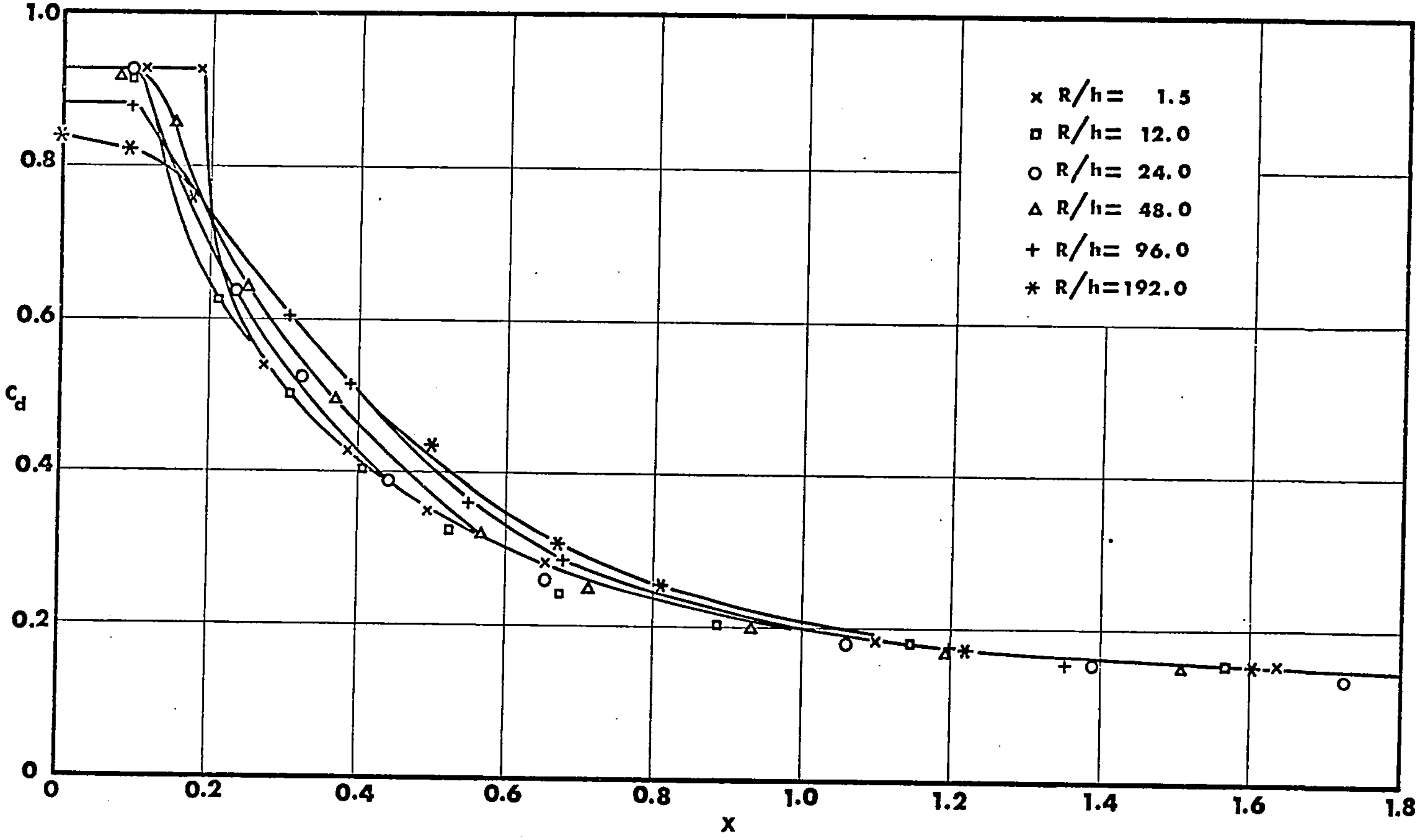

FIGURE 23 Variation of discharge coefficient with slenderness ratio for rotating vortex chamber

(R/a = 12.0)

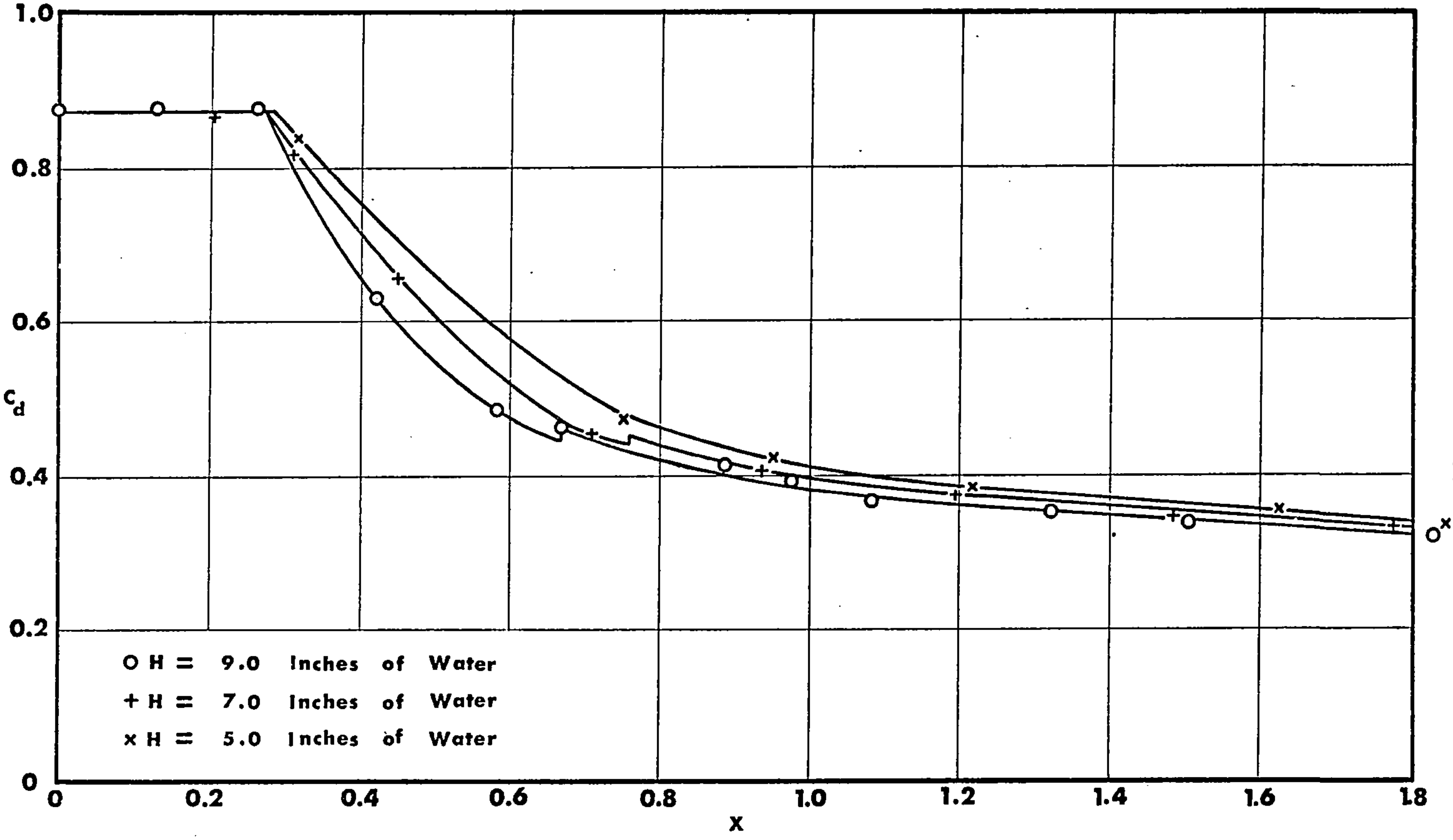

FIGURE 24 Variation of discharge coefficient with supply pressure head for rotating vortex chamber

(R/a = 24.0, R/h = 12.0)

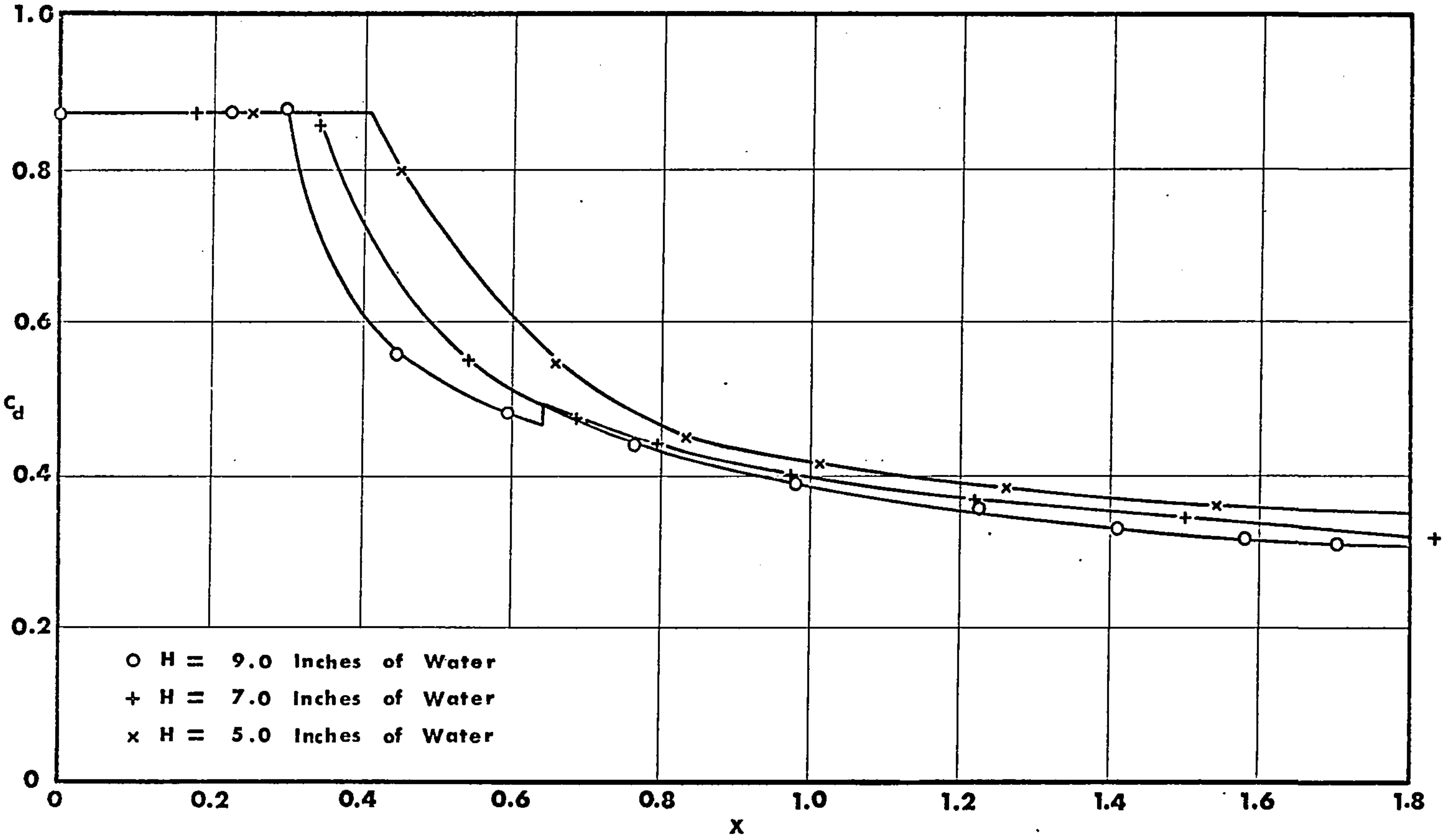

FIGURE 25 Variation of discharge coefficient with supply pressure head for rotating vortex chamber

(R/a = 24.0, R/h = 24.0)

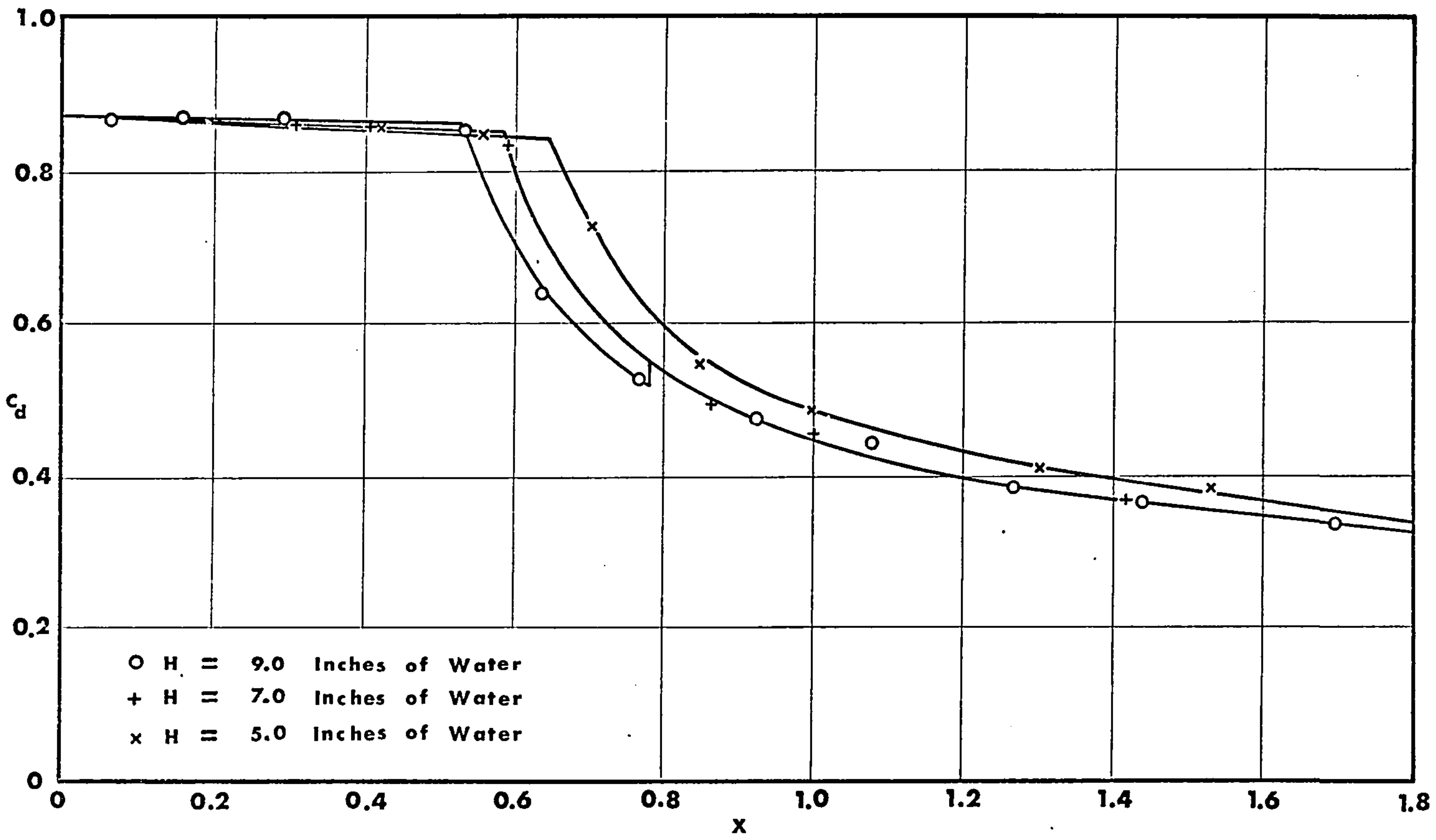

FIGURE 26 Variation of discharge coefficient with supply pressure head for rotating vortex chamber

(R/a = 24.0, R/h = 96.0)

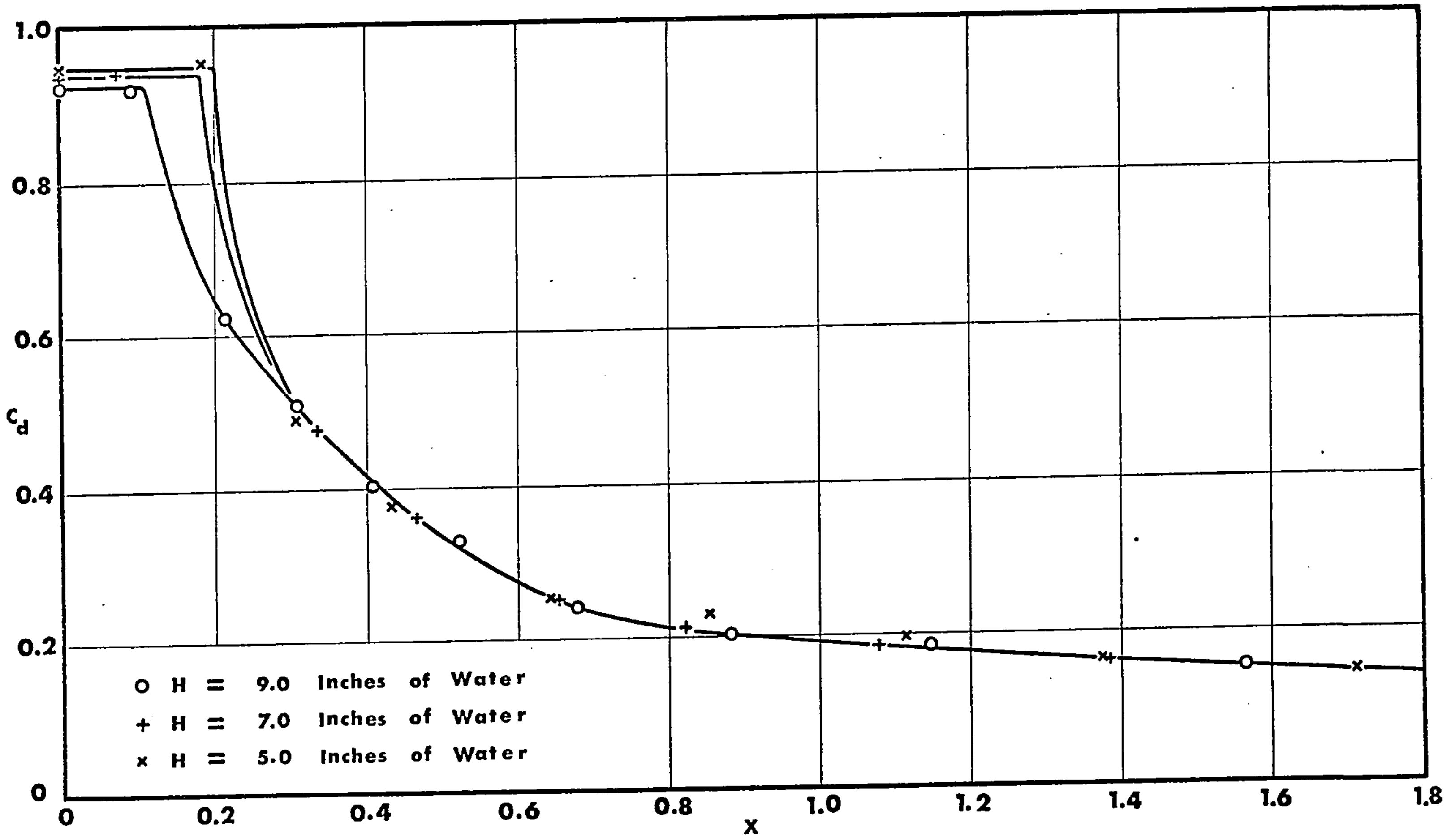

FIGURE 27 Variation of discharge coefficient with supply pressure head for rotating vortex chamber

(R/a = 12.0, R/h = 12.0)

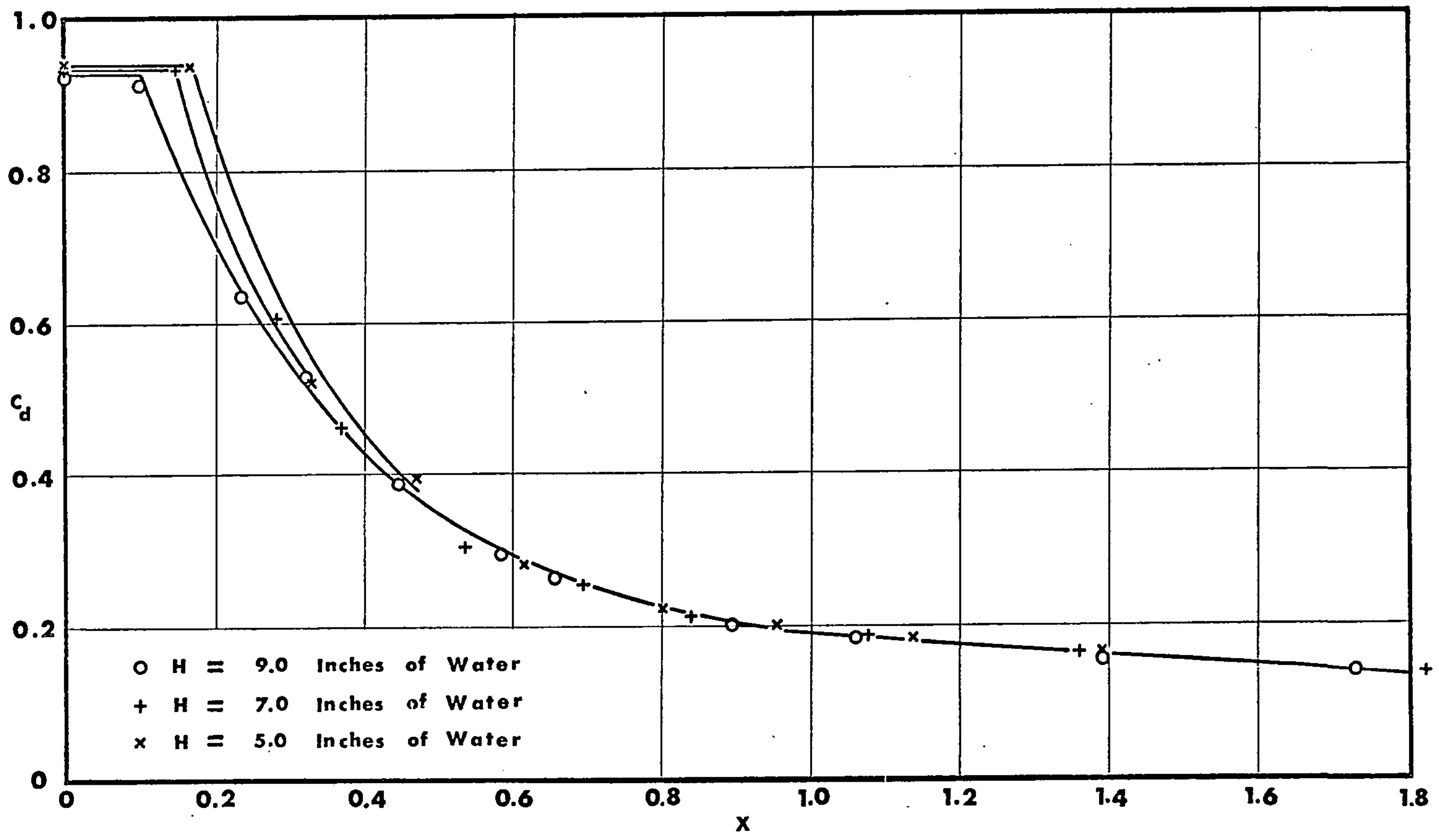

FIGURE 28 Variation of discharge coefficient with supply pressure head for rotating vortex chamber

(R/a = 12.0, R/h = 24.0)

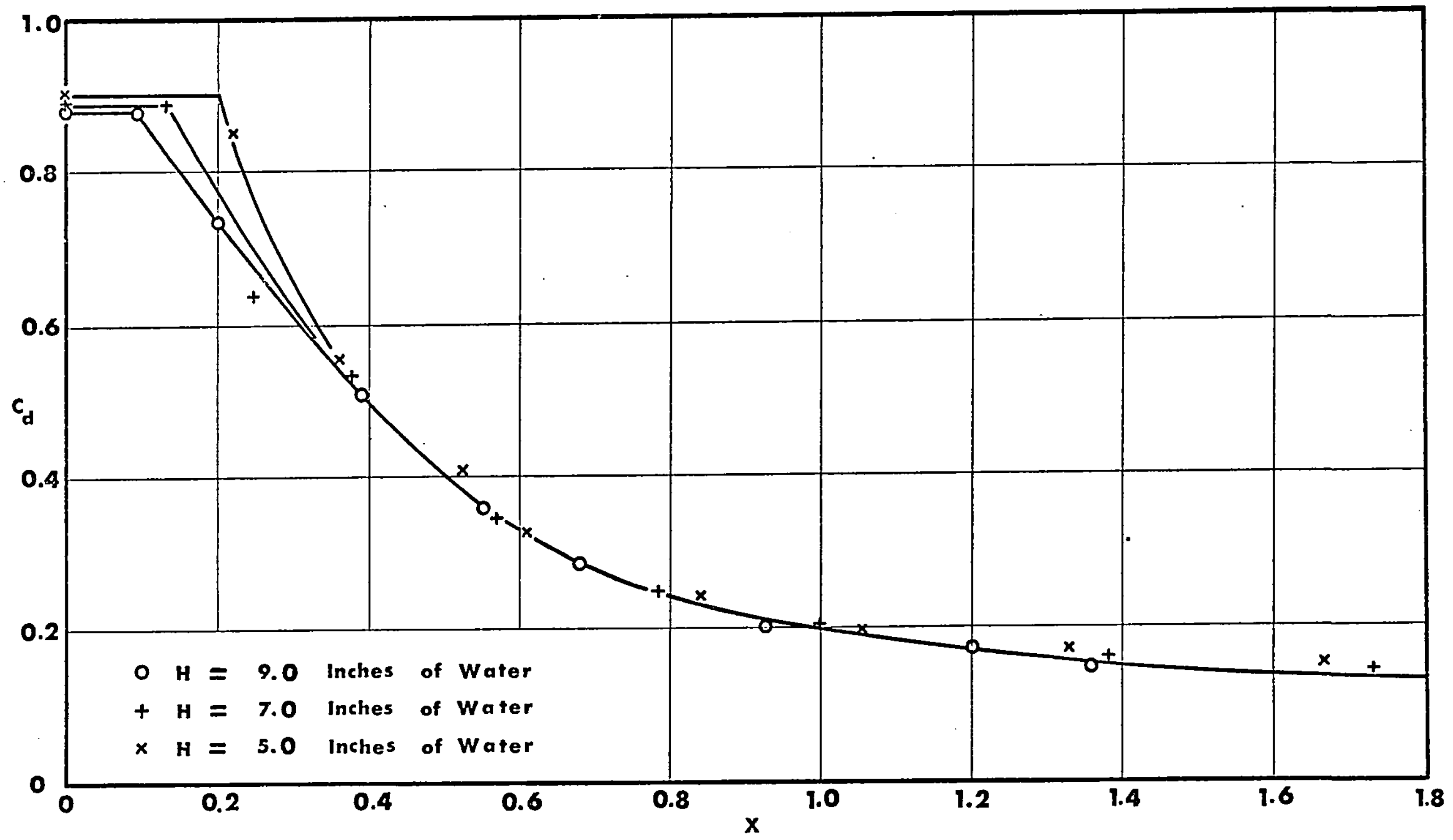

FIGURE 29 Variation of discharge coefficient with supply pressure head for rotating vortex chamber

(R/a = 12.0, R/h = 96.0)

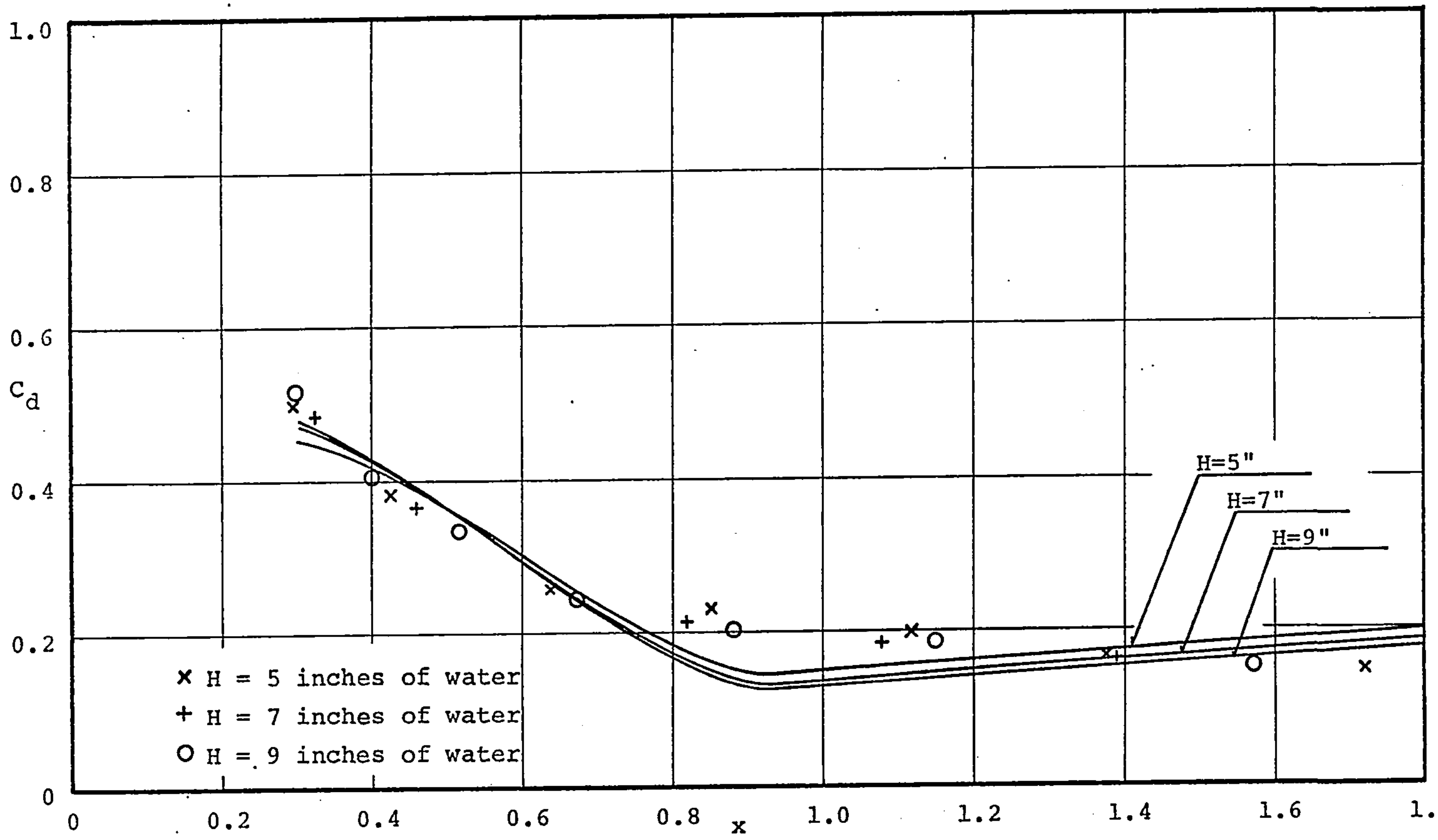

FIGURE 30 Comparison between theory and experimental results for the variation of discharge coefficient with supply pressure head

(R/a = 12, R/h = 12)

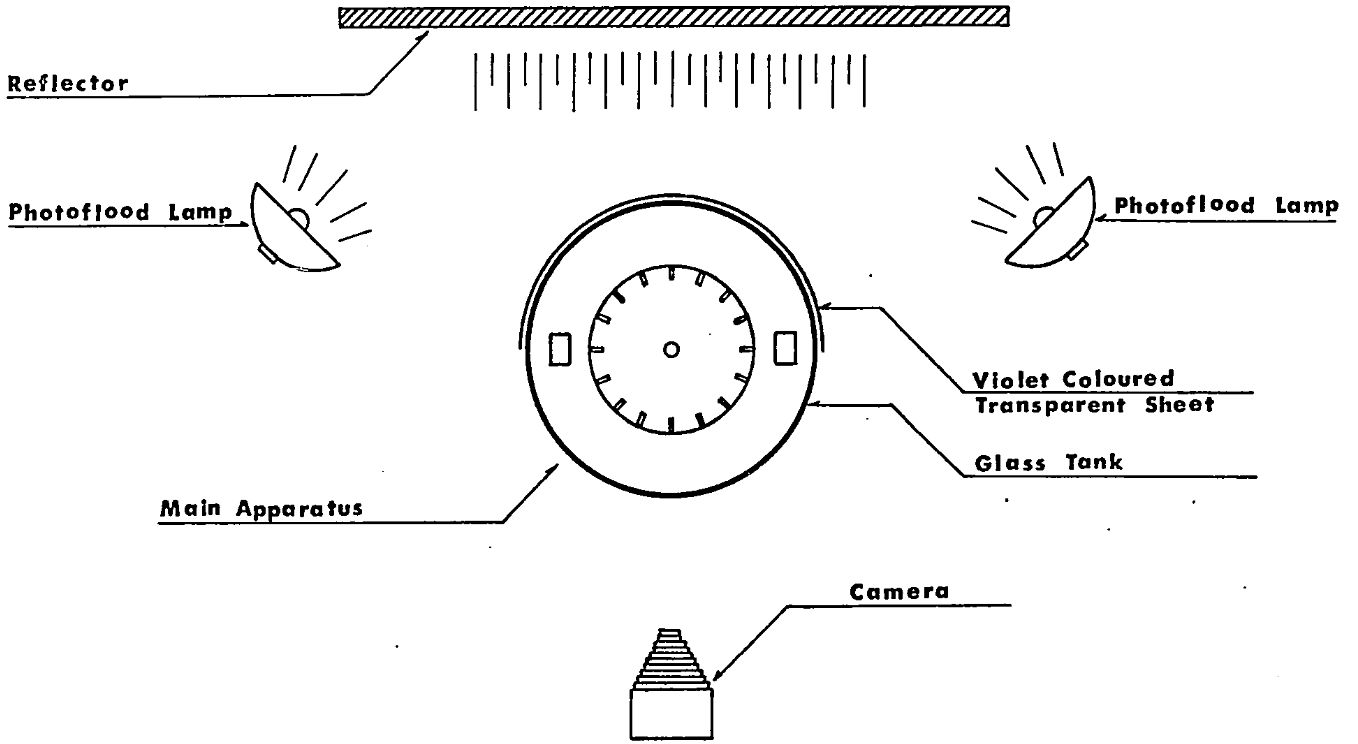

FIGURE 31 The Photographic arrangement for flow visualization

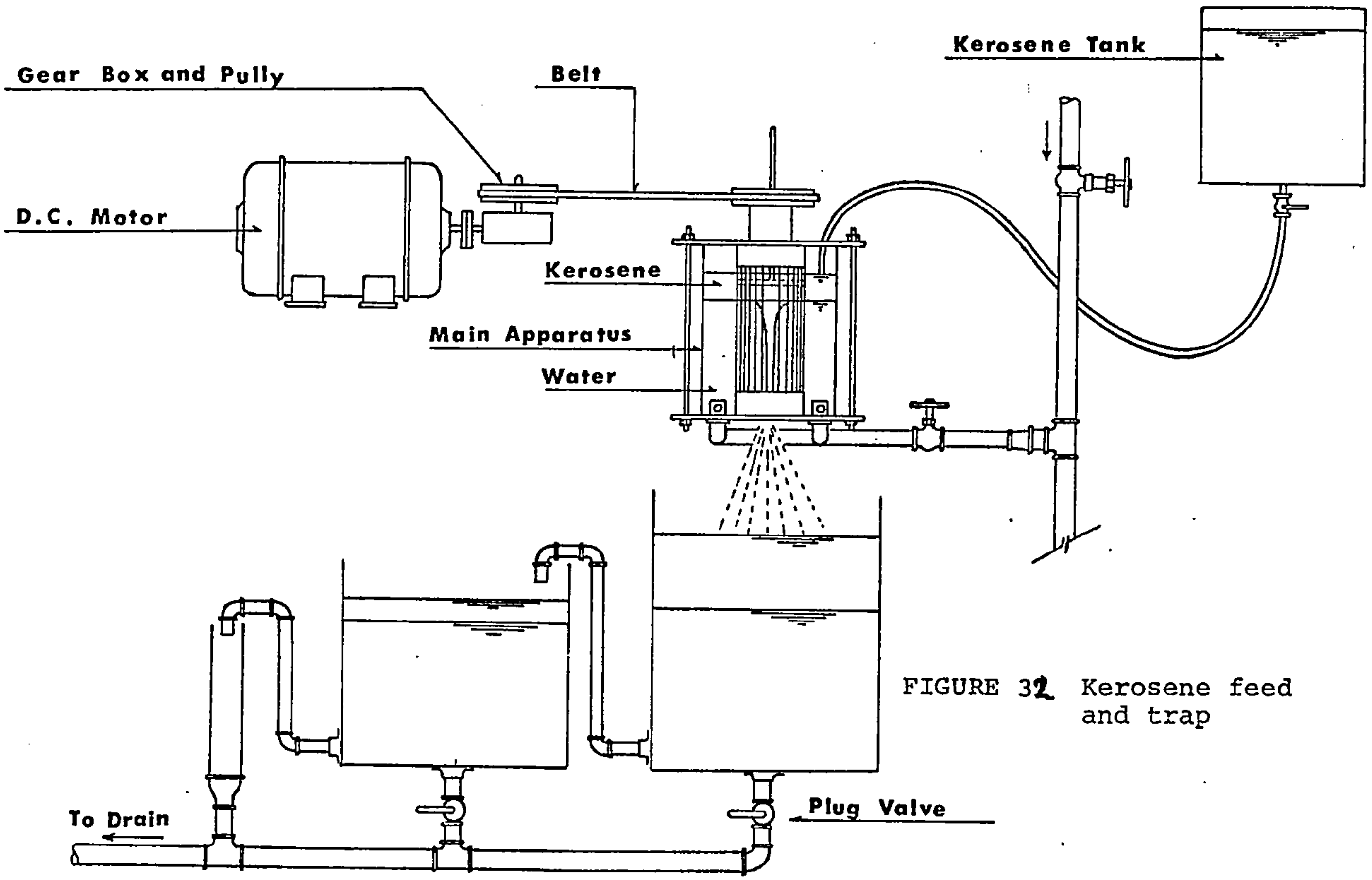

FIGURE 32 Kerosene feed and trap

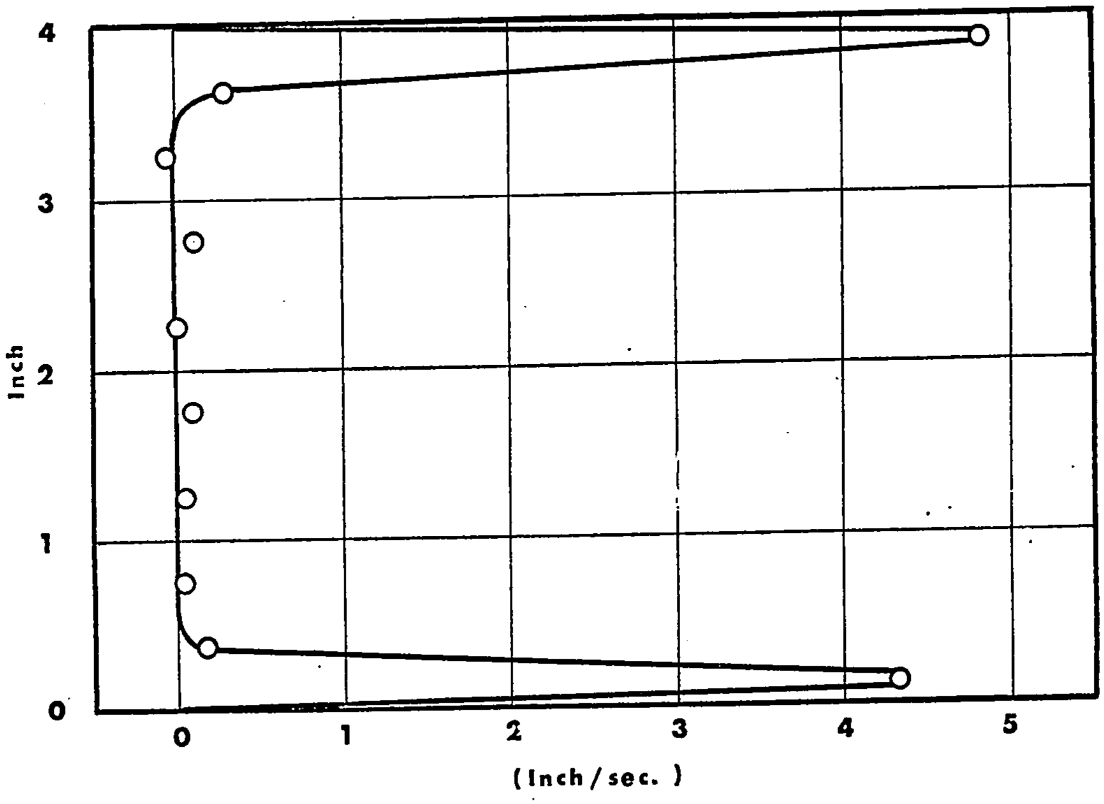

FIGURE 33 Radial velocity distribution at the outlet radius

(R/a = 24.0, R/h = 1.5 and X = 1.0)

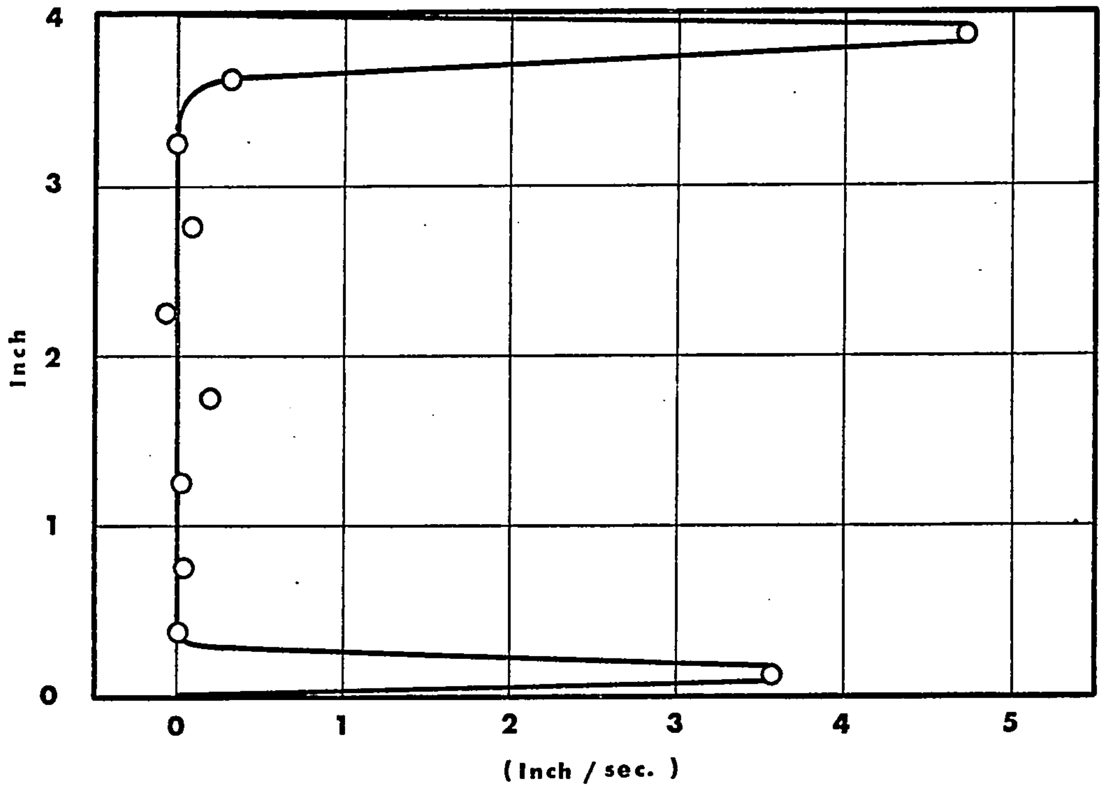

FIGURE 34 Radial velocity distribution at the outlet radius (R/a = 24.0, R/h = 1.5 and X = 1.5)

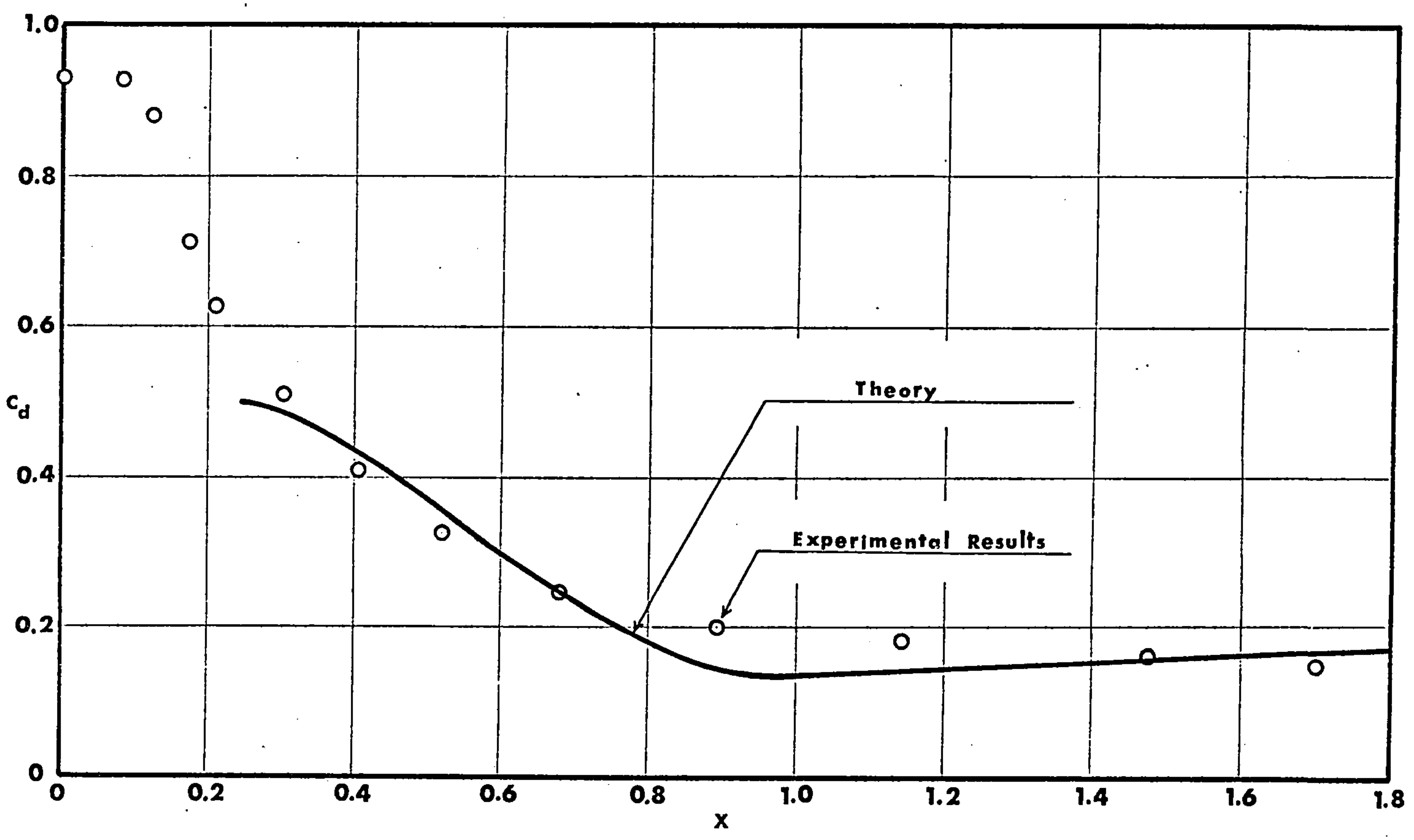

FIGURE 35 Comparison between theory and experimental results for rotating vortex chamber

(R/a = 12.0, R/h = 12.0)

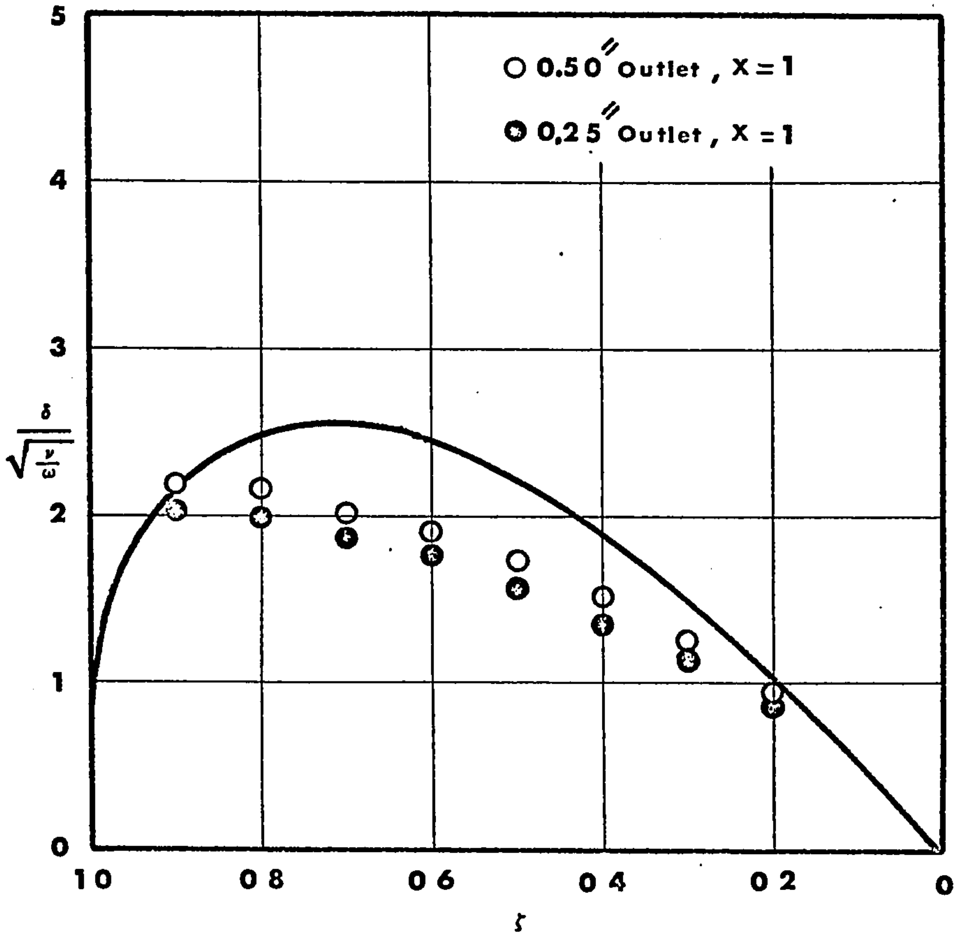

FIGURE 36 Comparison between theoretical and experimental boundary-layer profiles for rotating vortex chamber

PLATES

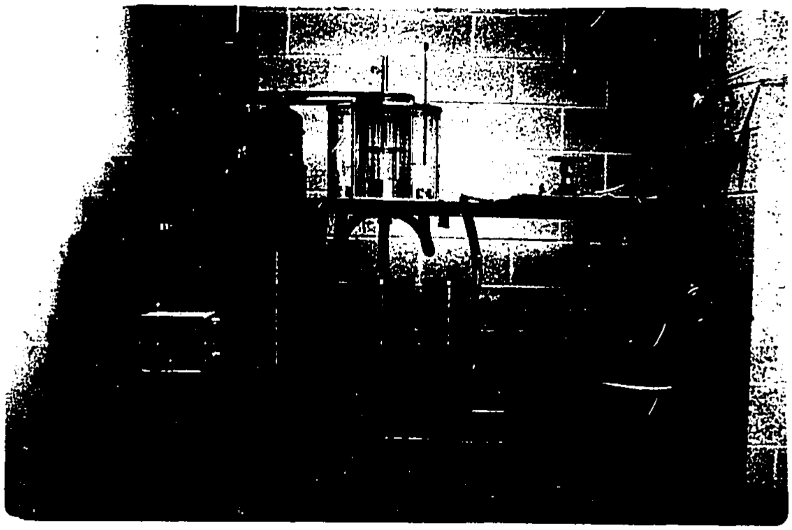

PLATE 1 General lay-out of the apparatus

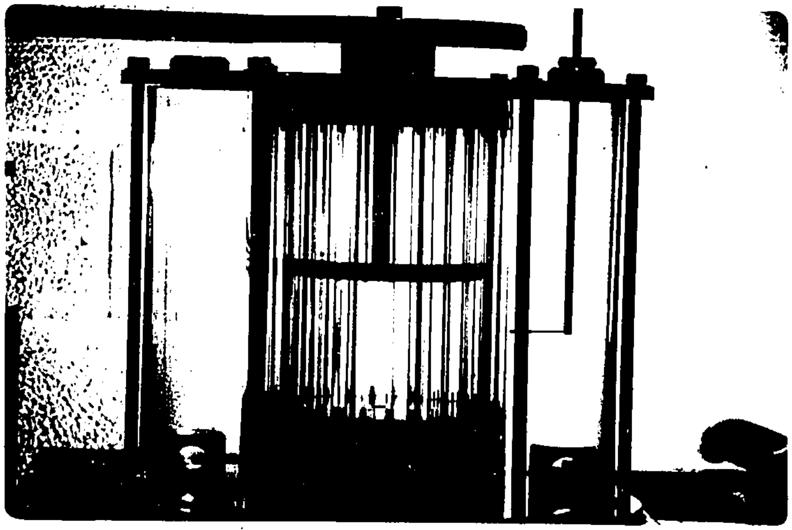

PLATE 2 Main apparatus

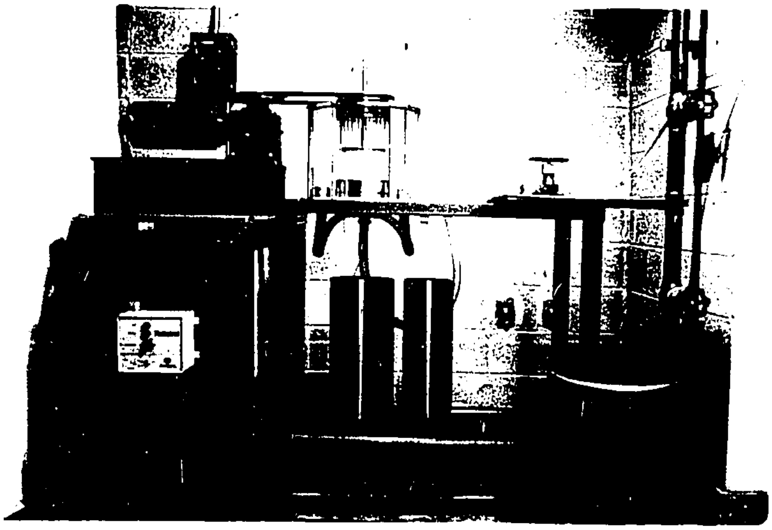

PLATE 1 General lay-out of the apparatus

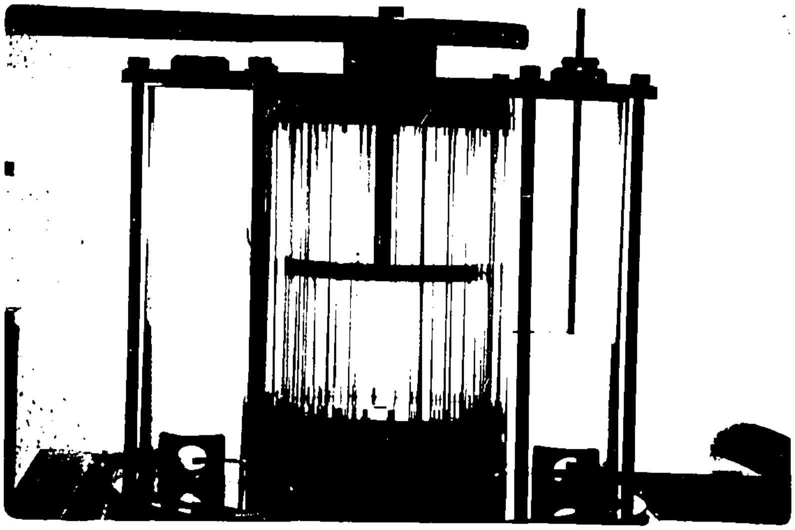

PLATE 2 Main apparatus

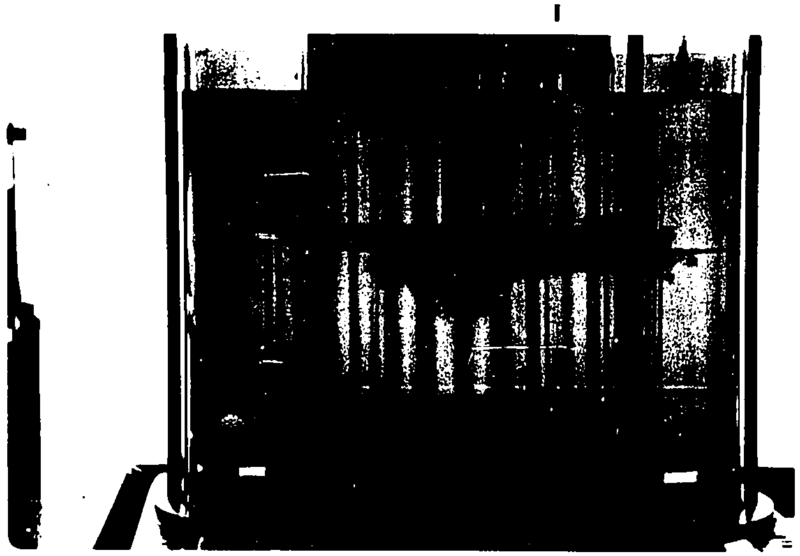

PLATE 3 Core flow (R/h = 1.5, R/a = 24.0 and X = 0.5)

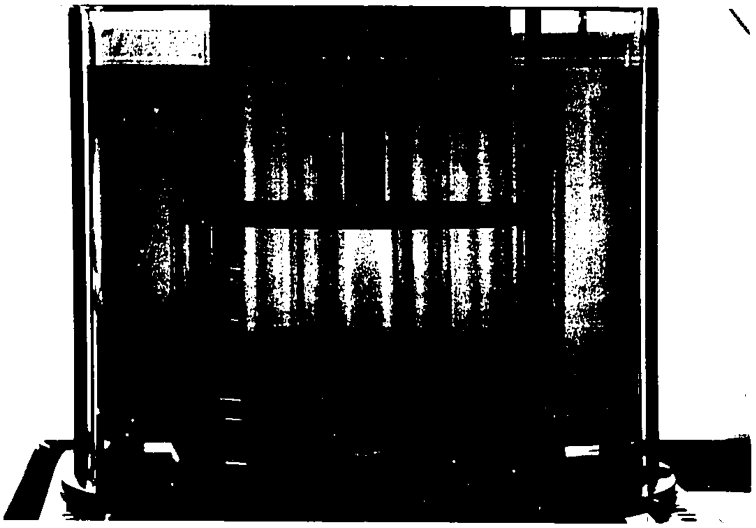

PLATE 4 Reverse flow (R/h = 1.5, R/a = 24.0 and X = 0.7)

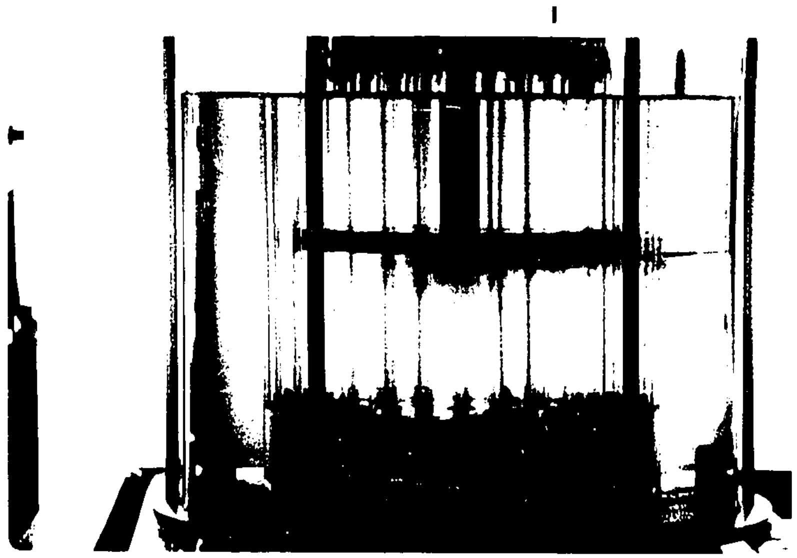

PLATE 3 Core flow ($R/h = 1.5$, $R/a = 24.0$ and $X = 0.5$)

PLATE 4 Reverse flow ($R/h = 1.5$, $R/a = 24.0$ and $X = 0.7$)

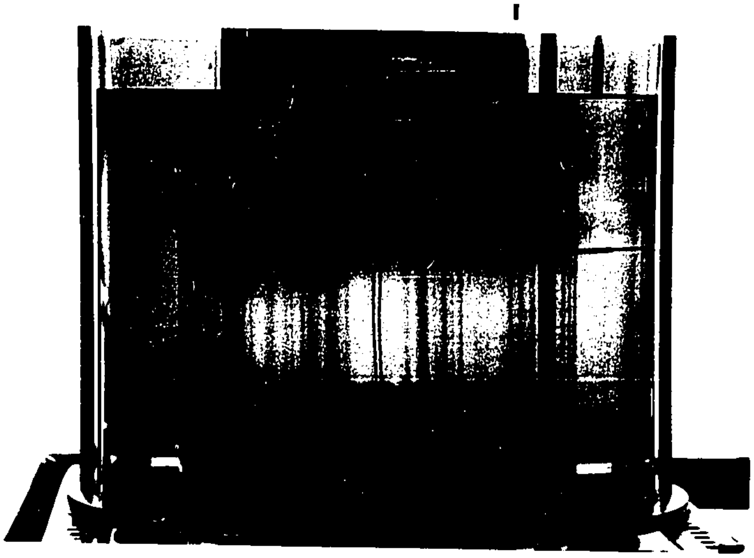

PLATE 5 Core flow around the air core (R/h = 1.5, R/a = 24.0 and X = 1.8)

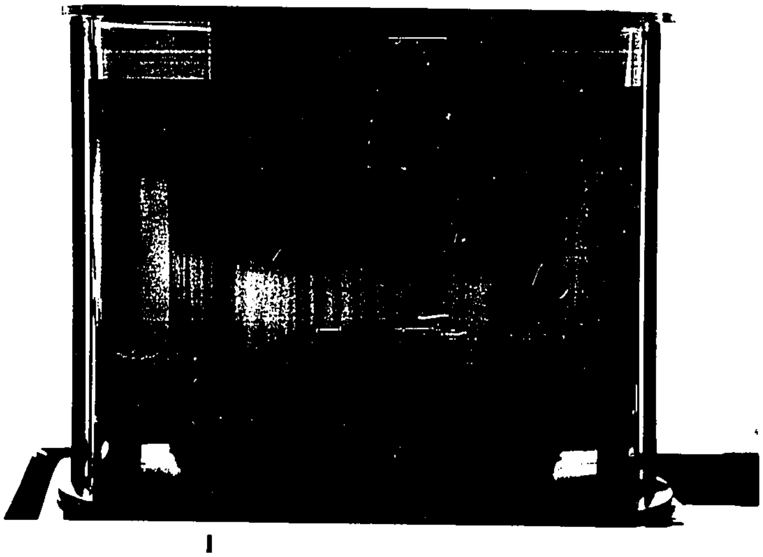

PLATE 6 Core flow around the air core (R/h = 1.5, R/a = 12.0 and X = 0.75)

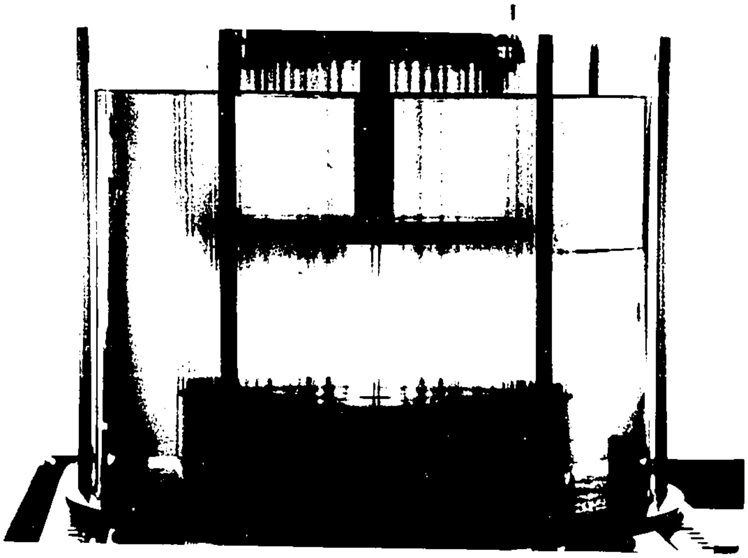

PLATE 5 Core flow around the air core (R/h = 1.5, R/a = 24.0 and X = 1.8)

PLATE 6 Core flow around the air core (R/h = 1.5, R/a = 12.0 and X = 0.75)

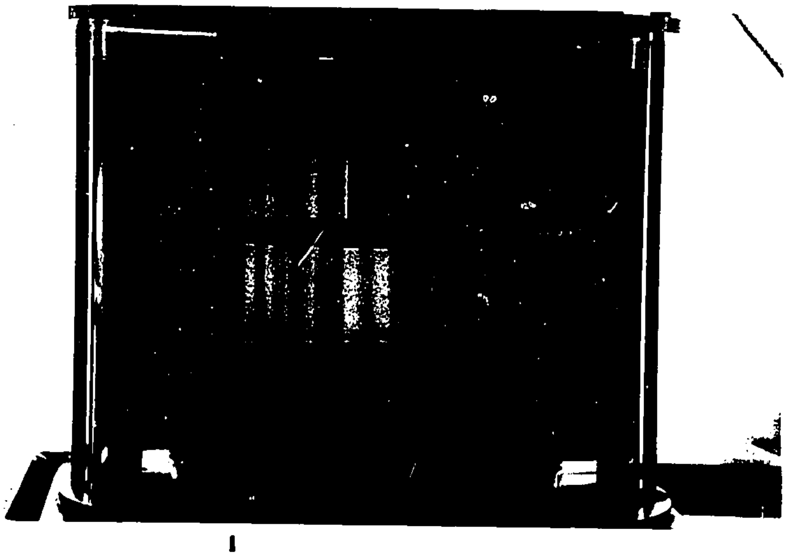

PLATE 7 Air core on its way up (R/h = 1.5, R/a = 12.0 and X = 0.5)

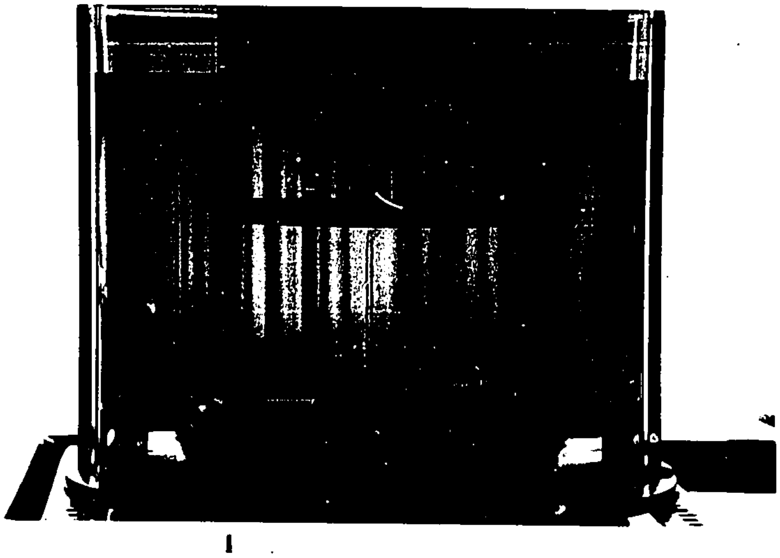

PLATE 8 Air core after being fully developed (R/h = 1.5, R/a = 12.0 and X = 0.5)

PLATE 7 Air core on its way up (R/h = 1.5, R/a = 12.0 and X = 0.5)

PLATE 8 Air core after being fully developed (R/h = 1.5, R/a = 12.0 and X = 0.5)

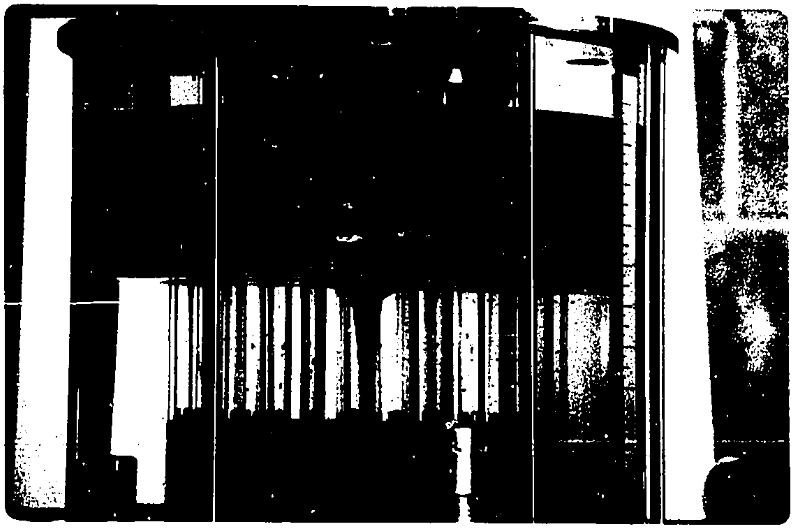

PLATE 9 Two-liquid flow

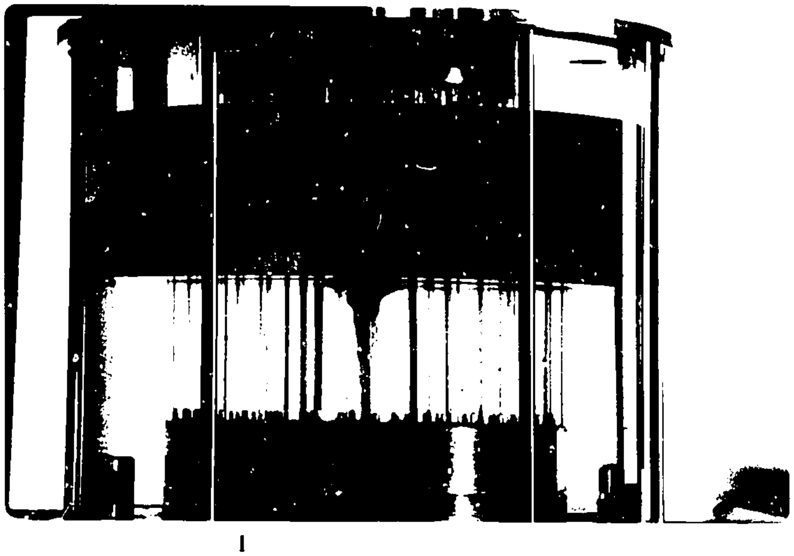

PLATE 9 Two-liquid flow